minerals

MDPI

Article

Coupled Microstructural EBSD and LA-ICP-MS Trace Element Mapping of Pyrite Constrains the Deformation History of Breccia-Hosted IOCG Ore Systems

Samuel Anthony King [1,*], Nigel John Cook [1], Cristiana Liana Ciobanu [1], Kathy Ehrig [1,2], Yuri Tatiana Campo Rodriguez [1,3], Animesh Basak [4] and Sarah Gilbert [4]

[1] School of Chemical Engineering, The University of Adelaide, Adelaide, SA 5005, Australia; nigel.cook@adelaide.edu.au (N.J.C.); cristiana.ciobanu@adelaide.edu.au (C.L.C.); kathy.ehrig@bhp.com (K.E.); yuri.camporodriguez@adelaide.edu.au (Y.T.C.R.)
[2] BHP Olympic Dam, 10 Franklin Street, Adelaide, SA 5000, Australia
[3] Geosciences Institute, Graduate Program in Geology, University of Brasília, Brasília 70910-900, DF, Brazil
[4] Adelaide Microscopy, The University of Adelaide, Adelaide, SA 5005, Australia; animesh.basak@adelaide.edu.au (A.B.); sarah.gilbert@adelaide.edu.au (S.G.)
* Correspondence: samuel.king@adelaide.edu.au

Abstract: Electron backscatter diffraction (EBSD) methods are used to investigate the presence of microstructures in pyrite from the giant breccia-hosted Olympic Dam iron–oxide copper gold (IOCG) deposit, South Australia. Results include the first evidence for ductile deformation in pyrite from a brecciated deposit. Two stages of ductile behavior are observed, although extensive replacement and recrystallization driven by coupled dissolution–reprecipitation reaction have prevented widespread preservation of the earlier event. Laser ablation inductively coupled plasma mass spectrometry (LA-ICP-MS) element maps of pyrite confirm that many pyrite grains display compositional zoning with respect to As, Co, and Ni, but that the zoning is often irregular, patchy, or otherwise disrupted and are readily correlated with observed microstructures. The formation of ductile microstructures in pyrite requires temperatures above ~260 °C, which could potentially be related to heat from radioactive decay and fault displacements during tectonothermal events. Coupling EBSD methods with LA-ICP-MS element mapping allows a comprehensive characterization of pyrite textures and microstructures that are otherwise invisible to conventional reflected light or BSE imaging. Beyond providing new insights into ore genesis and superimposed events, the two techniques enable a detailed understanding of the grain-scale distribution of minor elements. Such information is pivotal for efforts intended to develop new ways to recover value components (precious and critical metals), as well as remove deleterious components of the ore using low-energy, low-waste ore processing methods.

Keywords: electron backscatter diffraction; pyrite; olympic dam; microstructures; low-angle subgrain boundaries; ductile deformation; compositional zoning

Citation: King, S.A.; Cook, N.J.; Ciobanu, C.L.; Ehrig, K.; Campo Rodriguez, Y.T.; Basak, A.; Gilbert, S. Coupled Microstructural EBSD and LA-ICP-MS Trace Element Mapping of Pyrite Constrains the Deformation History of Breccia-Hosted IOCG Ore Systems. *Minerals* **2024**, *14*, 198. https://doi.org/10.3390/min14020198

Academic Editors: Glenn Bark and Alan R. Butcher

Received: 15 January 2024
Revised: 9 February 2024
Accepted: 13 February 2024
Published: 15 February 2024

1. Introduction

Pyrite (FeS_2) is the most common sulfide mineral in the Earth's crust. It is sufficiently refractory to allow the preservation of microstructures that are typically erased in more ductile ore minerals, meaning it can be used to fingerprint sequential stages in the deformational history of a mineral deposit [1]. Pyrite is therefore a valuable indicator of deformation in sulfide ore deposits [2], and it has been widely used to characterise metamorphosed ores and successfully constrain the impact of regional metamorphism and associated deformation on mineralization [3–6].

Early studies viewed pyrite as a mineral with brittle behavior at most crustal conditions, transitioning to ductile behavior at temperatures above ~425 °C [7–9]. The application of electron backscatter diffraction (EBSD) techniques to pyrite underpinned major

improvements in understanding pyrite deformation mechanisms [5,10–12]. This research culminated in construction of a new deformation mechanism map for pyrite [13] that indicates ductile behavior down to temperatures as low as ~260 °C. Ductile deformation in pyrite is commonly accommodated through low-angle subgrain boundary formation by dislocation creep during dislocation glide with a climb recovery step operated through slip on {100} and, less commonly, {110} systems [3,10,11]. However, deformation style largely depends on the mineralogy and fabric of the surrounding groundmass, whereby a ductile or very fine matrix can allow uninterrupted dislocation glide without grain locking or formation of low-angle boundaries [5].

Pyrite is also an important carrier of minor and trace elements, with a capacity to preserve geochemical signatures and compositional zonation through post-formational overprinting events [14–18]. Trace and minor elements are either incorporated in lattice-bound (solid solution) form or as nanoparticles. Several recent studies [19–23] have documented the importance of crystal defects as traps for trace elements, thus confirming theoretical approaches first put forward more than three decades ago [24]. In addition, the ability of pyrite to respond to strain and the mechanism of deformation may further control not only incorporation but also the retention or release of trace elements [25]. Among common trace elements in pyrite, often heterogeneously distributed within intracrystalline zoning patterns, are gold and several 'critical metals', notably cobalt and nickel (e.g., [26]). A microstructural analysis of pyrite can therefore lead to not only a better appreciation of how the ore formed and evolved over geological time but can also represent a valuable tool in efforts to understand how these minor, potential by-product elements are distributed and/or remobilized at the grain-scale.

This contribution focuses on new microstructural data for pyrite from the giant (>10 billion tonne) Olympic Dam hematite-dominant Cu-U-Au-Ag deposit, South Australia [27]. Olympic Dam is the largest uranium deposit and largest iron–oxide copper-gold (IOCG) deposit on Earth [28] and is widely considered an archetype for IOCG mineralization. It is also by far the largest ore system in the major metallogenic belt known as the Olympic Cu-Au Province [29]. High-precision ID-TIMS U-Pb hematite geochronology [30] has provided an unequivocal age of 1591.27 $\pm$ 0.89 Ma for mineralization and confirmed a magmatic–hydrothermal origin, with mineralizing fluids sourced from contemporaneous Hiltaba suite granites. Mineralogical, geochronological, and structural studies over the past two decades have recognized the impact of several post-Mesoproterozoic tectonothermal events on the deposit and the broader Olympic Cu-Au Province. The Olympic Dam deposit exhibits a systematic deposit scale zonation expressed by variation in the speciation of Cu-Fe-sulfides and proportions of different gangue minerals [28]. Irrespective of mineral zone, the sulfide assemblage is recognized as being dominantly of hypogene origin.

Contemporary opinion is that the gross architecture of the deposit and its inherent mineralogical zoning is largely a preserved, primary feature. Nevertheless, pervasive fluid-assisted modification of the ore assemblage has taken place over the past 1.6 billion years and may have been assisted by a continuous supply of radiogenic heat. Despite widespread replacement textures, nanoscale investigation of Cu-Fe-sulfides from Olympic Dam [31] has shown evidence of primary textures between bornite and chalcocite group minerals, interpreted as exsolutions along multiple cooling paths from primary bornite solid solution $\leq$400 °C. The complexity of sulfide assemblages at the smallest scale and significance of overprinting events in reshaping the micron-scale distribution of elements of interest, even when the overall structure of the system is for the most part preserved, is illustrated clearly in a recent nanoscale study of gold-bearing pyrite from Olympic Dam [32]. These authors provide evidence for modification of oscillatory zoning patterns in pyrite by dissolution–reprecipitation processes and the syn-deformational remobilization of trace elements that led to release of lattice-bound gold to form trapped Au- and Au-Ag-Te nanoparticles. Moreover, the presence of pore-attached nanoparticles [32] suggests high percolation rates, the redistribution of Pb and Bi, and possibly a degree of scavenging of Au by Bi-bearing melts. This complexity in pyrite is complemented by recognition of new

sulfide growth and development of low-angle slip dislocations, twist-wall boundaries, and deformation-dipole nanostructures.

Despite the potential of EBSD to constrain the evolution of mineral textures, only limited EBSD work had been undertaken on Olympic Dam ores prior to the present study. Macmillan et al. [33] used EBSD evidence to interpret compositionally zoned uraninite as the result of a sequence of overprinting. The crystal–plastic deformation of uraninite was found to take place via formation and migration of defects and dislocations into tilt boundaries. The utility of EBSD for depicting superimposed events was illustrated by a map of an apparent single grain of chalcopyrite that was shown to be a fused aggregate with boundary domains harboring elevated concentrations of radiogenic lead (Figure 13 in Rollog et al. [34]).

The present study therefore sets out to expand on the evolution of sulfide assemblages at Olympic Dam and assess the impact that different deformation episodes have had on microscale trace element distributions. The EBSD-driven approach targeting microstructures in pyrite and associated phases is complemented by reflected light microscopy, scanning electron microscope (SEM) imaging and mapping, and quantitative trace element analysis by laser ablation inductively coupled plasma mass spectroscopy (LA-ICP-MS). While recognizing that ore textures, mineral compositions, and microstructures can show multiple overprints, EBSD is better suited for constraining deformation episodes and their sequences in some cases, despite poor preservation and heterogeneous expression of such events across the deposit.

Alongside our primary focus on EBSD analysis, we aim to understand the deformational evolution of pyrite by correlating the observed microstructures with internal compositional patterning defined by the grain-scale distribution of trace and minor elements as mapped by LA-ICP-MS. Linking the two methodologies serves two additional purposes. Firstly, efficient comminution benefits from understanding deformation-induced microstructures that are otherwise invisible. Secondly, accurate tracking of minor ore components of value (Au, Ag), or potential value (e.g., Co) through processing is contingent on a comprehensive appreciation of their distributions at the grain-scale (e.g., [35]), especially considering the critical interplay between pyrite textures and metallurgical performance [36,37].

2. Deposit Geology and Sample Suite

The world-class Olympic Dam Cu-U-Au-Ag deposit is part of the Olympic Cu-Au IOCG province located on the eastern edge of the Archean to Mesoproterozoic Gawler Craton [38] (Figure 1). Mineralization across the province was contemporaneous with formation of the Gawler silicic large igneous province (SLIP) (~1.595–1.586 Ga; [39]), which comprises Gawler Range volcanics (GRV) and the bimodal magmatic Hiltaba Suite (HS) [40,41]. At Olympic Dam, the HS granitoids and GRVs unconformably overlie older basement Hutchinson Group metasedimentary units, Donington suite granitoids (~1.86–1.85 Ga; [42]) and Wallaroo Group Meta(volcanic)sediments (~1.76–1.74 Ga; [43]) (Figure 1).

The orebody is hosted entirely in the Olympic Dam Breccia Complex (ODBC; Figure 2; [44]), in turn located within the Roxby Downs Granite (RDG) from which it is derived. The host RDG becomes increasingly altered and brecciated inwards towards the center of the deposit [45–47]. Hematite, the main product of Fe-metasomatism, can be as high as >90% in some areas of the deposit. This includes barren hematite quartz ± barite breccias in the shallow central part of the deposit (HEMQ), which are defined by <0.08 wt% Cu, trace concentrations of sulfide minerals, and a lack of aluminosilicates. The RDG is shown to have been initially emplaced at depths of 6–8 km [45,47]. High-precision ID-TIMS U-Pb hematite geochronology provided an age of 1591.27 ± 0.89 Ma for the earliest mineralization, just ~2 Ma later than the latest magmatic zircon in the RDG (1593.28 ± 0.26 Ma; [30]). Uplift and cupola collapse of the RDG at 2–3 km is proposed to have triggered brecciation and ore formation [48].

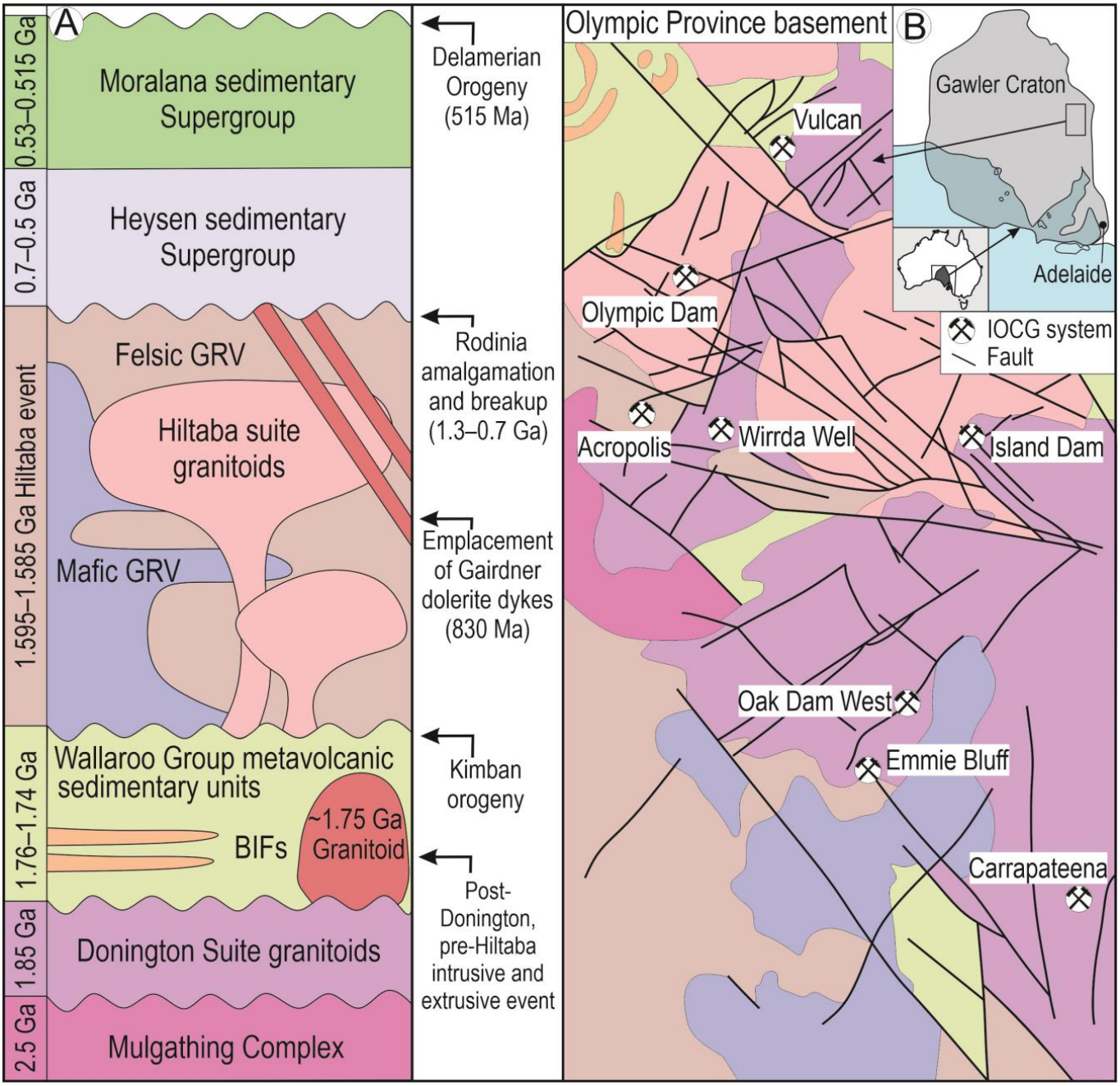

Figure 1. (**A**) Generalized stratigraphic column that depicts relationships between basement and cover rocks in the Olympic Dam district and major tectonothermal events, BIF–banded iron formation. (**B**) Geological map of the district showing major faults and IOCG systems superimposed onto basement geology. Modified after Courtney-Davies et al. [30].

The structural evolution of the Olympic Dam region is a response to major tectonic events, notably the breakup of the Nuna supercontinent in the ~300 Ma following initial mineralization, amalgamation, and subsequent break-up of Rodinia (~1.3–1.1 Ga and ~0.85–0.6 Ga, respectively), and then amalgamation to Gondwana (~0.6–0.3 Ga). Unroofing of the deposit occurred during formation of Rodinia prior to ~1425 Ma deposition of the Pandurra Formation. The Olympic Province was further affected by far-field effects from the 1.4–1 Ga Grenville Orogeny [49] and/or the 1.3–1.2 Ga Musgrave Orogeny [50], as well as emplacement of the Gairdner LIP and associated dolerite dykes [51] (Figure 1). The formation of the Adelaide Rift Basin was associated with several stages of rifting, hydrothermal activity and deposition of the Stuart Shelf sedimentary succession that consists of the Heysen and Moralana Supergroups across the Olympic Province [52] (Figure 1). The Delamerian Orogeny across South Australia (514–490 Ma; [53]) resulted in extensive faulting and veining across the region.

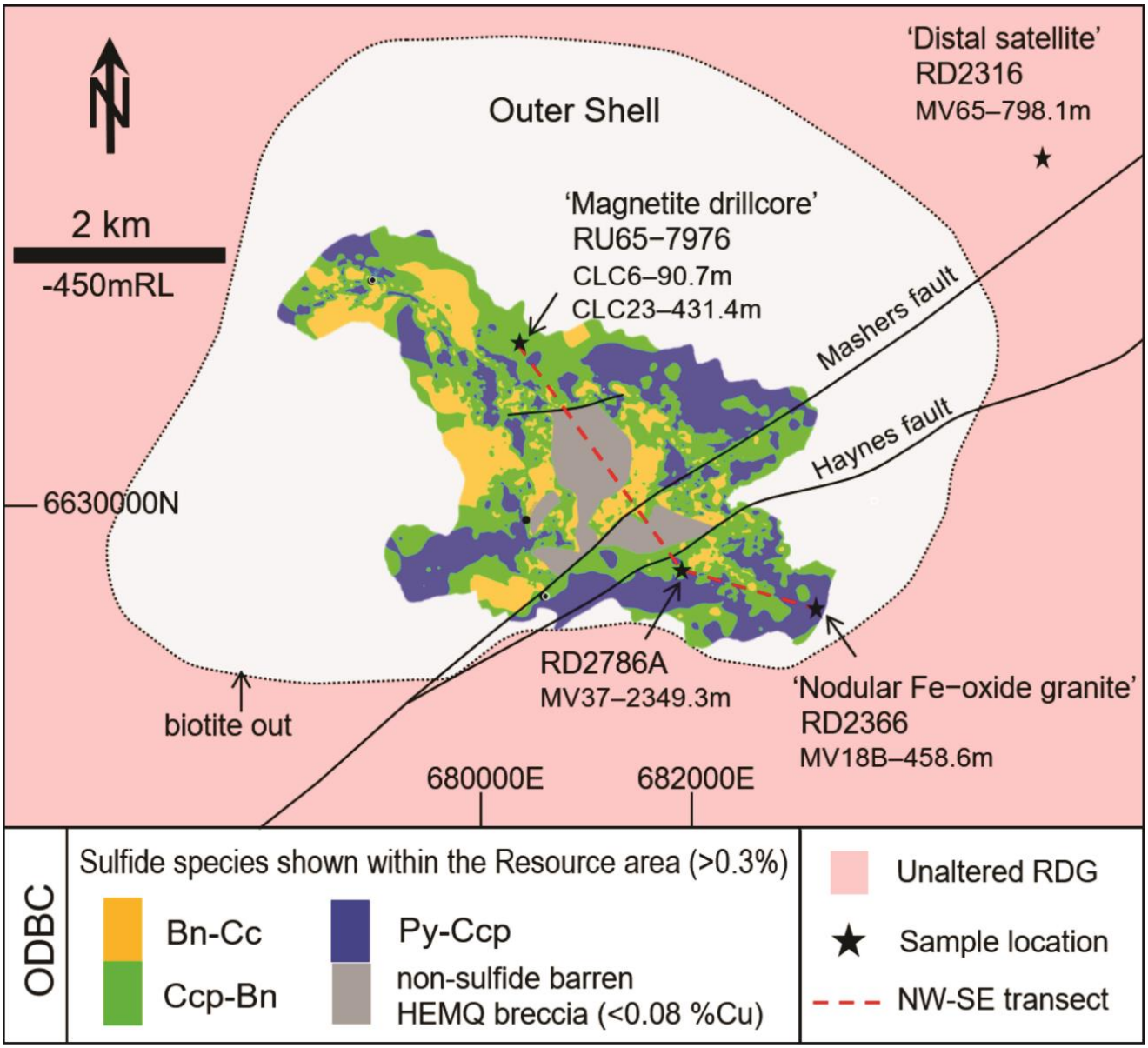

Figure 2. Geological sketch map of the Olympic Dam deposit modified after Ehrig et al. [28] showing zoning with respect to Cu-Fe-sulfide mineralogy: pyrite–chalcopyrite (Py-Ccp), chalcopyrite–bornite (Ccp-Bn) and bornite–chalcocite (Bn-Cc) within the Olympic Dam Breccia Complex (ODBC). Annotations: RDG—Roxby Downs Granite, HEMQ—hematite quartz ± barite breccia.

At the periphery of the orebody is a weakly altered/brecciated granite called the "outer shell" [49] (Figure 2), which is characterized by the presence of magnetite and pyrite–chalcopyrite assemblages that formed during early-stage alteration. This pyrite–chalcopyrite zone develops systematically inwards and upwards to zones defined by bornite–chalcopyrite and bornite–chalcocite mineralogy, into the HEMQ [28,54] (Figure 2). There is a close association between Cu mineralization and Fe-oxides across the NW lobe, core margin and SE lobe of the orebody, whereas Cu mineralization is sporadic in the Fe-oxide rich core. Across the NW lobe and center of Olympic Dam mineralization is observed to depths of ~1000 m, while in the SE lobe south of the Masher's fault (Figure 2), Cu-Fe-sulfides extend vertically to depths of at least ~2500 m. Pockets of mineralization occur outside the main resource perimeter within less altered RDG (Figure 2). This 'Distal satellite' mineralization displays a pyrite–chalcopyrite sulfide assemblage resembling that in the outer shell.

EBSD work was undertaken on five samples containing assemblages considered representative of pyrite in assemblages within the outer shell (three drillholes along a ~3.5 km-long transect and the Distal satellite; Figure 2). Irrespective of the sample's placement across the deposit, all are representative of the deep pyrite–chalcopyrite zone in the "outer shell". The transect crosses the NW lobe from which two samples (CLC6 and CLC23) were studied, across the SE lobe (MV37) and extends to the SE lobe outer shell (MV18B) (Table 1; Figure 2). A sample from the Distal satellite (MV65) was also chosen for this study. A spectrum of breccias with variable proportions of Fe-oxides and matrix were included: (i) dominant hematite/magnetite (CLC 6 and CLC23) (Figure 3A); (ii) siderite-rich, milled rock flour breccia (MV18B) (Figure 3B); (iii) quartz–chlorite, sulfide-poor breccia (MV37) (Figure 3C); and (iv) altered granite with pyrite veins (MV65) (Figure 3D) and are further described in Table 1.

Table 1. Samples investigated in this study, locations, and brief descriptions.

Deposit Area	Drillhole	Length along Drillhole (M)	Sample	Analysis	Description
Middle (core margin)	RU65-7976a (magnetite drillcore)	90.7	CLC6	EBSD, LA-ICP-MS	Disseminated pyrite as large aggregates or fragments in breccias with hematite clasts and as fine-grained matrix. The latter also comprises minor chalcopyrite and gangue minerals.
		431.4	CLC23	EBSD	
SE lobe-outer shell	RD2366 (nodular Fe-oxide granite drillcore)	458.6	MV18B	EBSD, LA-ICP-MS	Pyrite and chalcopyrite as fine stringers in rock flour, siderite-rich, hematite breccia. Further explanation is given in [48].
SE lobe	RD2786A	2349.3	MV37	EBSD, LA-ICP-MS	Fine-grained pyrite within fractures crosscutting quartz and chlorite domains showing slight deformation in a hematite breccia.
Distal satellite	RD2316	798.1	MV65	EBSD	Coarse pyrite grains and/or aggregates along fractures in altered granite; minor chalcopyrite and hematite present.

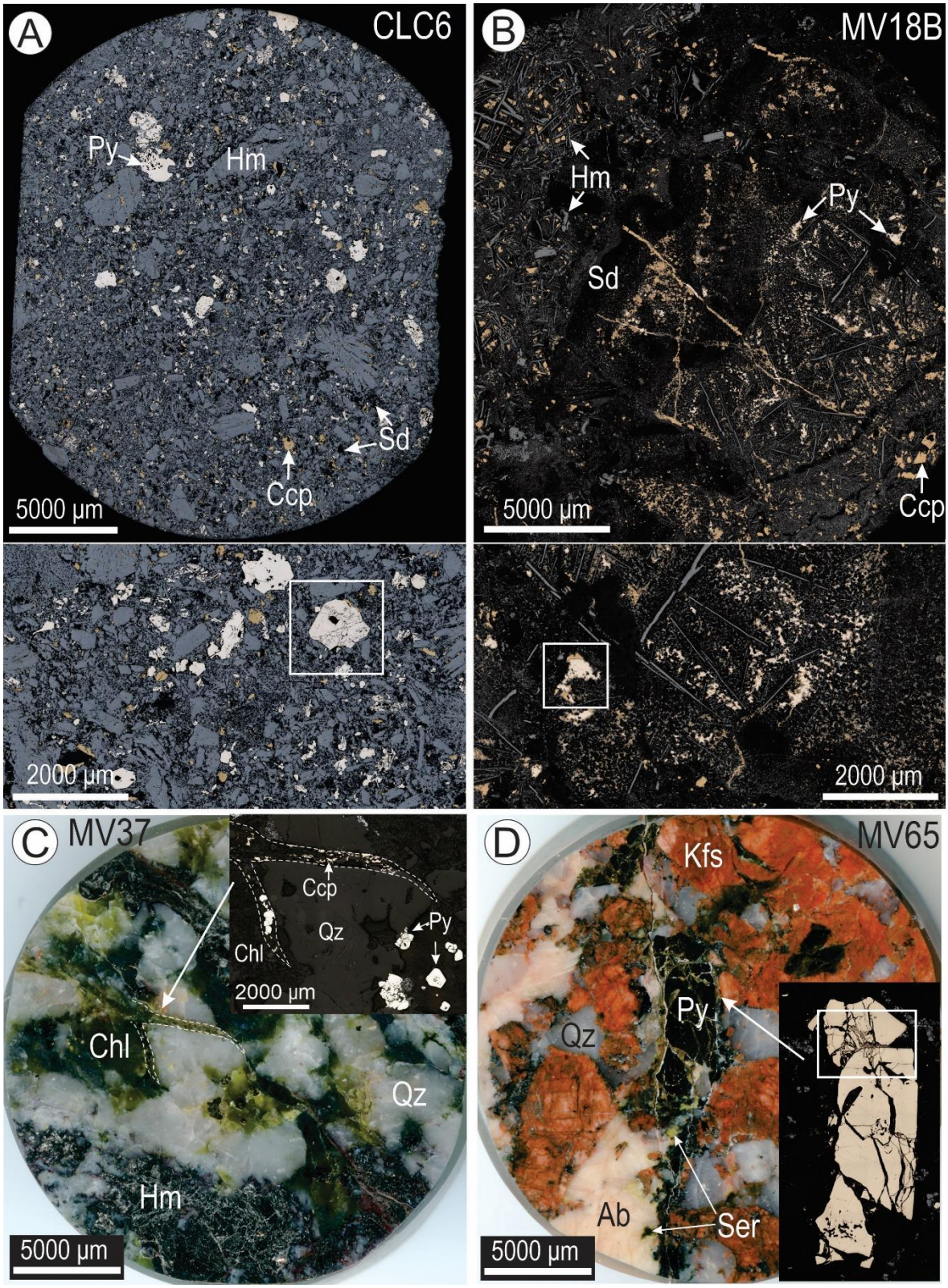

Figure 3. Overview reflected light maps (**A**,**B**) and scanned images (**C**,**D**) of analyzed polished blocks with assemblages and pyrite textures described in Table 1. The assemblage in CLC23 is closely analogous to that of CLC6. White boxes shown on the insets mark EBSD maps of pyrite. Abbreviations: Ab—albite, Chl—chlorite, Ccp—chalcopyrite, Hm—hematite, Kfs—K-feldspar, Py—pyrite, Qz—quartz, Sd—siderite, Ser—sericite.

3. Analytical Methodology

Assemblages containing pyrite grains were identified and texturally characterized at the micron-scale in reflected light and imaged on a FEI Quanta 450 scanning electron microscope (SEM) operated in backscattered electron (BSE) mode. This reconnaissance work also enabled selection of suitable grains for subsequent EBSD and trace element analysis by LA-ICP-MS.

EBSD data was collected on two SEM platforms: a FEI Helios NanoLab "Dualbeam" FIB/SEM platform; and a Hitachi SU1510, both housed at Adelaide Microscopy, The University of Adelaide. The two instruments utilize Oxford Symmetry S3 detectors (Oxford Instruments, Abingdon, UK). Prior to analysis, each sample was polished in a suspension of colloidal silica for 1 h and a thin (~2.5 nm) coat of carbon was applied. Energy-dispersive X-ray spectroscopy (EDS) was also used alongside EBSD data collection using an Oxford Ultim Max Large Area SSD EDS detector (Oxford Instruments) operating at an accelerating voltage of 20 kV and beam current of 2.7 nA. Orientation contrast (OC) data was processed in AZtecCrystal (Oxford Instruments) to produce band contrast (BC), inverse pole figure (IPF) denoted X-, Y-, or Z-based on crystallographic orientation, texture component (TC), and grain rotation orientation deviation (GROD) angle maps. Post-processing was used to reduce noise by applying a "wildspike" correction, gentle clean-up steps and appropriate pseudosymmetry corrections.

LA-ICP-MS trace element mapping was conducted on three pyrite grains that were previously studied by EBSD (Table 1). Over the grains, sets of parallel lines were ablated using a RESOlution-SE 193 nm Excimer laser coupled to an Agilent 8900x quadrupole ICP-MS (Agilent Technologies Australia. Mulgrave, VIC, Australia) also housed at Adelaide Microscopy. Laser spot size varied between 7 and 10 µm, depending on grain size, and operated at a pulse repetition rate of 5 Hz and fluence of 3 J/cm^2. Twenty-three isotopes were measured: ^{27}Al, ^{34}S, ^{49}Ti, ^{51}V, ^{55}Mn, ^{57}Fe, ^{59}Co, ^{60}Ni, ^{65}Cu, ^{66}Zn, ^{75}As, ^{77}Se, ^{107}Ag, ^{111}Cd, ^{118}Sn, ^{121}Sb, ^{125}Te, ^{182}W, ^{197}Au, ^{206}Pb, ^{207}Pb, ^{208}Pb, ^{209}Bi. The external reference material STD-GL3 [55] was analyzed before, during, and after pyrite ablation. Collected ablation profiles formed a series of parallel line rasters across the grain that were compiled and processed using 'Iolite' software (v.3; Elemental Scientific, Melbourne, VIC, Australia) [56] to generate trace element intensity maps. Mapped intensities are scaled independently for each element to enhance different features; unless stated otherwise in figure captions, the scale used is logarithmic (10^n). ^{57}Fe was selected as the internal standard, assuming a stoichiometric FeS_2 composition.

4. Results

4.1. Pyrite Textures and EBSD Mapping

4.1.1. Distal Satellite

Pyrite from sample MV65 is characteristically coarse (up to several mm across) and fractured, sometimes displaying a "porphyroblast"-like morphology enclosed within a rigid matrix of quartz and K-feldspar (Figure 3D). The selected pyrite features a dense fracture network, hundreds of µm in width, infilled with chalcopyrite and gangue minerals, mostly sericite (Figure 4A). Fine-grained hematite is clustered outside pyrite within the same vein. At the pyrite–pyrite grain impingement (Figure 4A), these fractures radiate from the interface at which pyrite has been pulverized and milled into a fine rock flour. Pyrite contains rounded inclusions comprising coexisting chalcopyrite and pyrrhotite, and rarely cattierite, CoS_2, (with Co/Ni ~4.3) (Figure 4B,C).

Band contrast and Y-IPF mapping reveal no clear microstructures in the pyrite (Figure 5A,B) although, SEM-BSE imaging does reveal trails of µm-sized galena blebs close to the grain margin (inset Figure 5A). EBSD pole-figure analysis on pyrite outlined on the Y-IPF map does however display an apparent strong rotation (~16°) about a single <100> labelled D1 on Figure 5C. The grains associated with this rotation (light/dark blue in outlined pyrite Figure 5B) are isolated from the pyrite by chalcopyrite and sericite infill (Figure 4A) and consequently register as separate grains on orientation contrast mapping.

In Figure 5C, from the {100} positions of D1, a shift of all <100> axes in the same orientation are preserved and labelled D2. Pole figure analysis on pyrite grains external to outlined pyrite that exceed 1000 pixels on Figure 5B, thus removing any randomly oriented finer grains, show an approximate mutual orientation close to the termination of the D2 shift in the 'outlined pyrite' (Figure 5D).

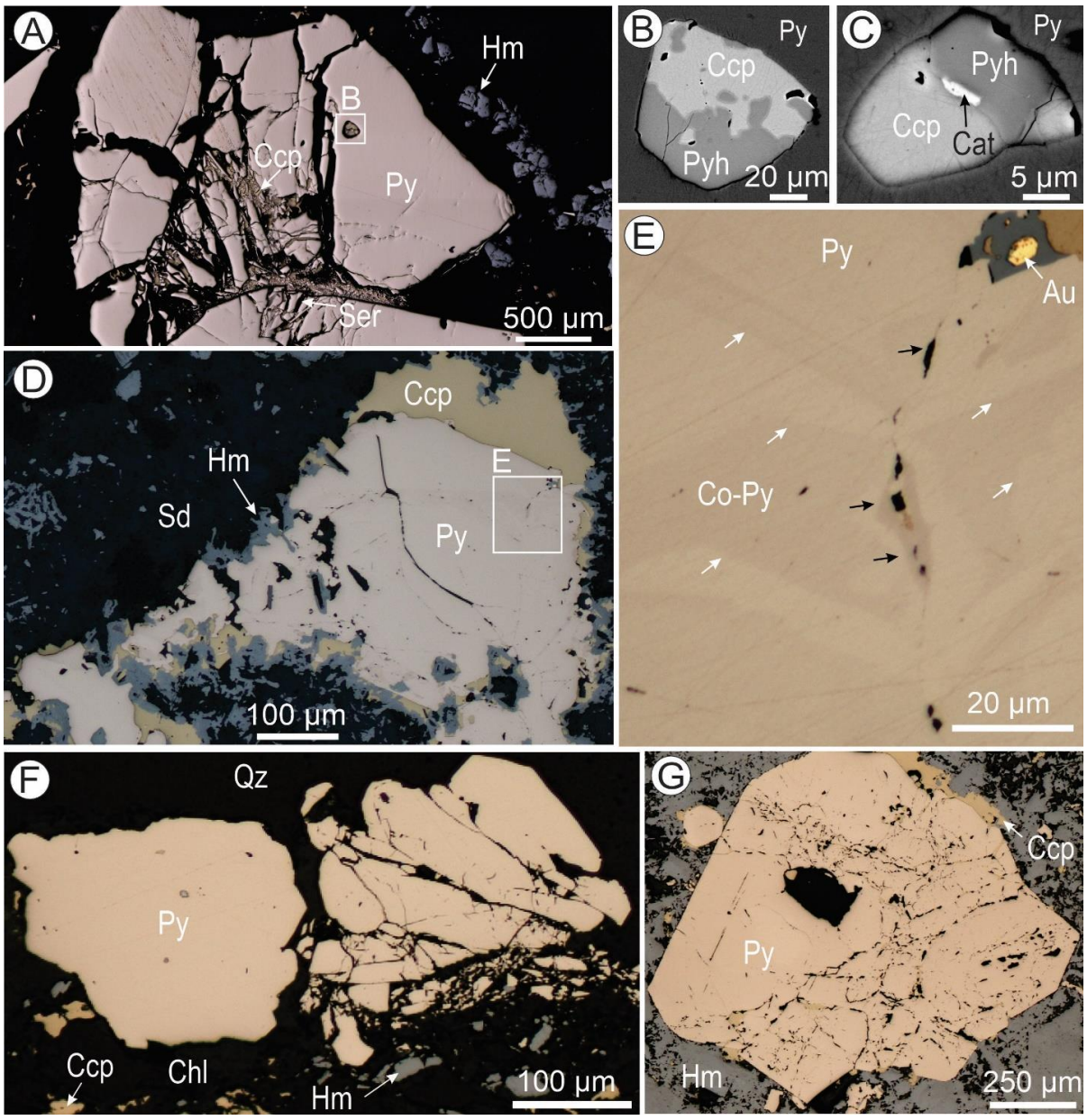

Figure 4. Reflected light and BSE images of pyrite grains selected for EBSD analysis. (**A**) Grain impingement in pyrite from sample MV65 with fracturing and pulverization to rock flour with (**B**,**C**) BSE images displaying rounded multiphase inclusions within pyrite. (**D**) Grain rich in healed fractures and inclusions of surrounding gangue from sample MV18B with white box depicting E. (**E**) Detail of grain from D, showing compositional zoning with respect to Co (white arrows) and presence of fine trails of gangue minerals (black arrows) that seem to offset pyrite zonation patterns. (**F**) Intact pyrite grain adjacent to a pulverized grain along a rupture in quartz from sample MV37. (**G**) Sub-idiomorphic highly pulverized pyrite grain from sample CLC6. Abbreviations: Au—native-gold, Cat—cattierite, Ccp—chalcopyrite, Chl—chlorite, Hm—hematite, Py—pyrite, Pyh—pyrrhotite, Qz—quartz, Sd—siderite, Ser—sericite.

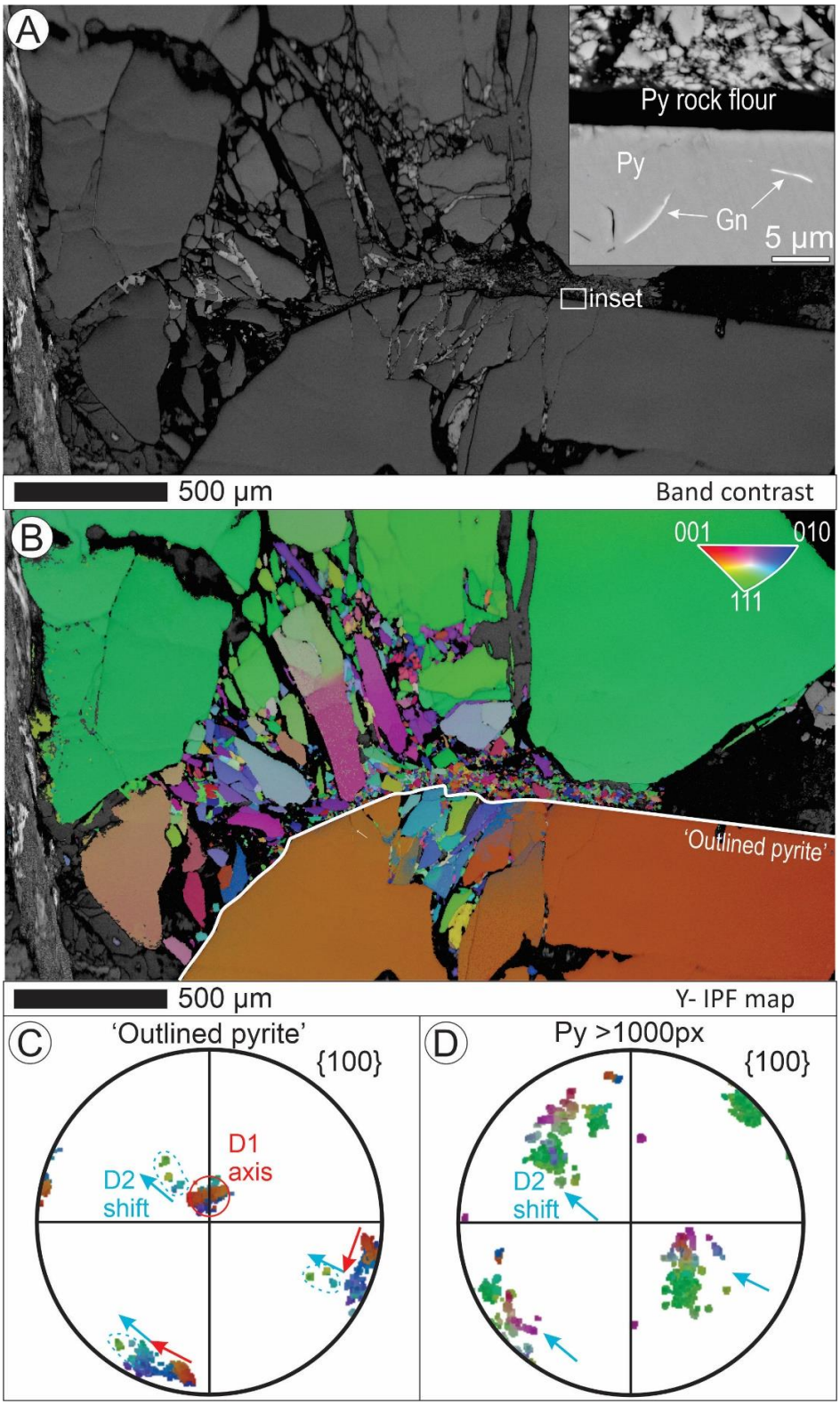

Figure 5. Orientation contrast EBSD maps and data from pyrite in sample MV65 (Figure 4A) (**A**) BC map with a BSE image inset displaying galena trails of sub-micron thickness at the grain margin. (**B**) Y-IPF map and corresponding (**C**,**D**) {100} pole figures with matching colors displaying pyrite orientations from (**C**) the outlined pyrite in B and (**D**) pyrite external to 'outlined pyrite' larger than 1000 pixels. Pole figures display two recognizable deformations, rotation about a <100> axis labelled D1, and a shift of all {100} axes labelled D2. Abbreviations: Gn—galena, Py—pyrite.

4.1.2. NW-SE Transect

One of the coarser pyrite grains within siderite-rich breccias was studied from sample MV18B (Figure 3B). Pyrite is mantled by fine-grained hematite and chalcopyrite, with embayment features characteristic of replacement by chalcopyrite (Figure 4D). Pyrite is characteristically zoned with respect to the distribution of Co, As and Ni (see Section 4.2), in a pattern that transitions from oscillatory near the grain margin to more patchy textures towards the grain center (Figure 4E). Fine structures that display Co enrichment around trails of chalcopyrite and siderite are also observed (Figure 4E).

In band contrast and GROD angle maps these structures are shown to have inflicted a small degree (2–5°) of misorientation to pyrite (Figure 6A,B). GROD angle mapping further reveals domains within pyrite that display different responses to deformation, separated by the major microstructure annotated '1'. Pyrite on the left of this microstructure shows subtle lattice distortion at the margins and a lenticular 'fish-shaped' region lined by fine trails that displays an 8° misorientation about a single <110> axis with surrounding pyrite (Figure 6B,C). The reflected light image shows this domain is at the margin of the Co-enriched zonation (Figure 6D). Pole figures from across the microstructure annotated '1' display a shift of all <100> axes (Figure 6E) that can only be attributed to fracture rotation. On the right of this structure, subtle lattice distortion is widespread and shows no correlation with the pyrite on the left (Figure 6B,F). In areas of pyrite 'bottlenecking' by surrounding gangue, this subtle misorientation locks into dislocations (Figure 6B,F) formed by distortion about multiple <100> axes, as shown in pole figures corresponding to '2' and '3' (Figure 6E), attributed to subgrain-boundary formation. There is also a close mutual orientation between pyrite and surrounding chalcopyrite (~1.5° misorientation), with chalcopyrite being uncharacteristically homogenous in this sample. The morphological and chemical heterogeneity of chalcopyrite and other Cu-Fe-sulfides across the deposit, and their response to deformation will be discussed in a subsequent paper.

Another fine-grained pyrite was analyzed from sample MV37 (Figure 3C inset). Pyrite displays varying degrees of brecciation, although some grains appear less impacted than others (e.g., the left grain in Figure 4F). In contrast to the aforementioned styles of pyrite texture, shear-induced deformation is suggested by pyrite domains comprising sets of low-angle, oblique fractures with fine-fragments of angular pyrite at the contact to the breccia matrix (Figure 4F). These fractures contain gangue and are associated with lower-order splintered fractures.

The BC map displays these finer microfractures well and confirms the presence of microstructures associated with an inclusion at the margin of the intact grain (Figure 7A). SEM-BSE imaging reveals that the pyrite 'inclusion' is bound by a zone with enhanced porosity; sub-µm-scale galena inclusions are observed along the microstructure (Figure 7B). The IPF map categorizes the microstructures as low- (2–5°) to mid-angle (5–8°) subgrain boundaries (Figure 7C), with the pole figure showing this lattice rotation occurred about a single <100> (Figure 7D). The pole figure also displays two distinct orientations that allow the inference of two original grains with a close mutual orientation. This is shown by the blue and red shades on the TC map (Figure 7E), which reveals an apparent embayment with no clear deformational response. BSE imaging at this contact (Figure 7F) does, however, show dense trails of quartz and galena, a feature sporadically observed elsewhere in the grain. The embayed fragment is severed from the bulk 'red' pyrite on the left of Figure 7E by gangue but exhibits a lower degree of misorientation than the proximal subgrains.

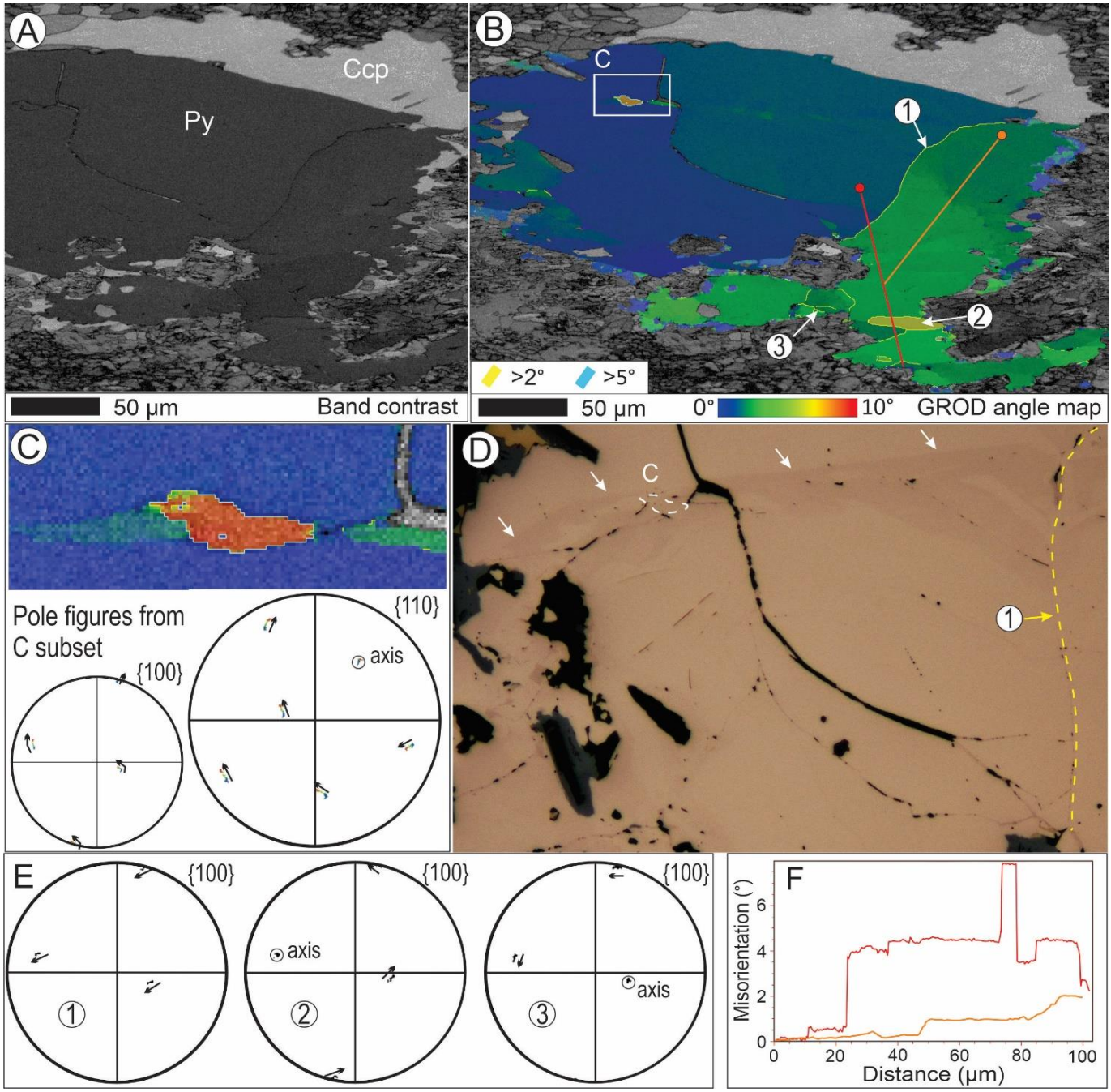

Figure 6. Orientation contrast maps and data from pyrite in sample MV18B (Figure 4D). (**A**) BC map and (**B**) GROD angle map that displays low- (yellow) and medium-angle (cyan) boundaries and progressive misorientation in pyrite. (**C**) A closeup of the medium-angle boundary domain that displays a lenticular morphology with corresponding {100} and {110} pole figures from the area. (**D**) Reflected light micrograph depicting the relationship between Co-As-Ni zonation (white arrows), the lenticular domain and microstructure 1 (yellow dotted line). (**E**) {100} pole figures taken across microstructures labelled 1, 2, and 3 shown on (**B**). (**F**) Transects (shown in (**B**)) taken across subtle misorientation (orange) and low-angle boundaries (red) show cumulative misorientation across the grain.

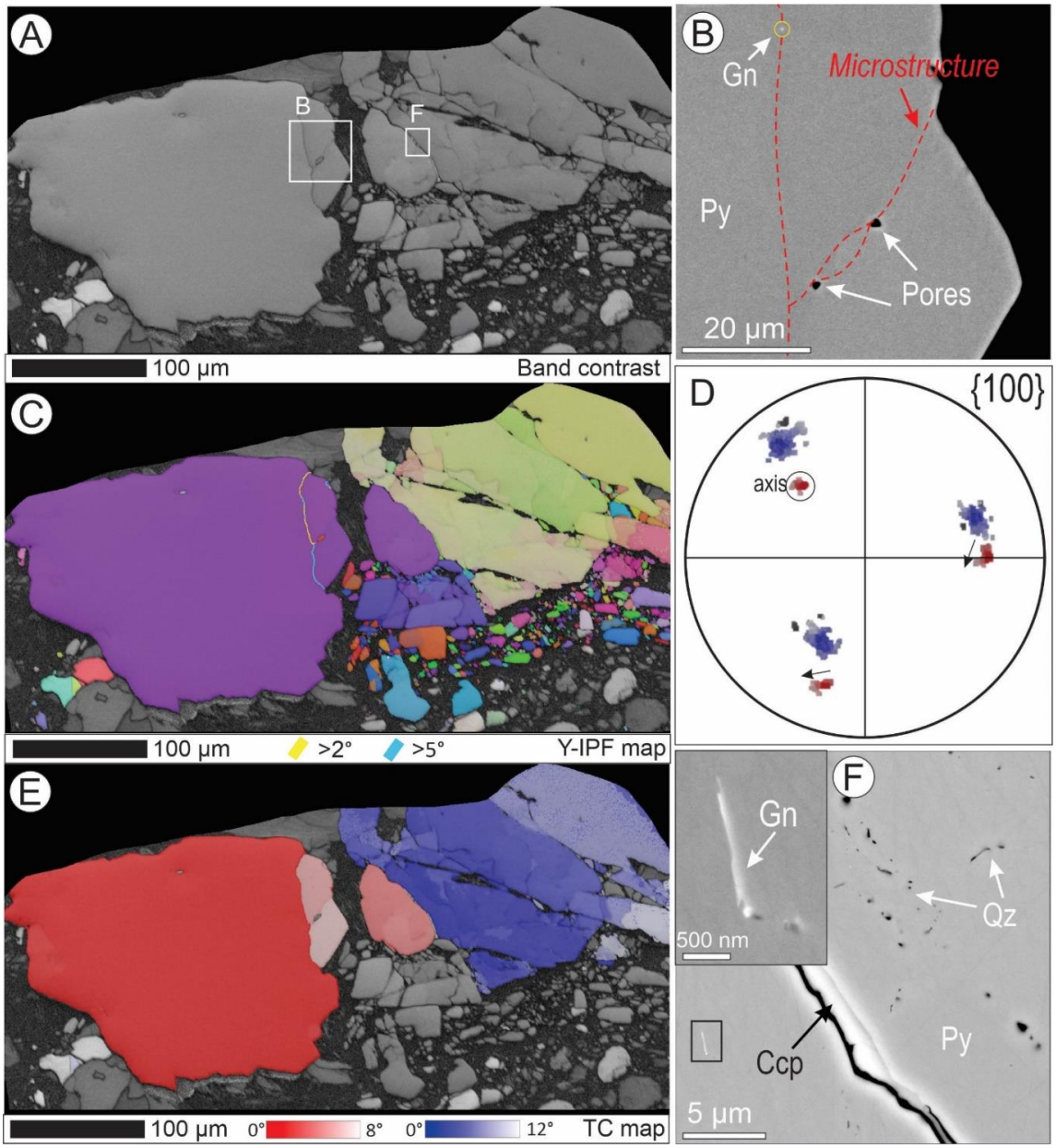

Figure 7. Orientation contrast maps and data from pyrite in sample MV37 (Figure 4F). (**A**) BC map displaying microstructures, (**B**) shown at higher magnification in BSE. (**C**) Y-IPF map displaying microfractures across the right grain with low- (yellow) and medium-angle (cyan) boundaries in the left grain. (**D**) {100} pole figure displaying rotation about a <100> axis with colors derived from (**E**) the TC map that shows two unique orientations. The red pyrite apparently impinges upon the blue, with a (**F**) closeup BSE image displaying quartz and galena trails at this margin. Ccp—chalcopyrite, Gn—galena, Qz—quartz.

Pyrite grains of variable size (~50 µm and ~750 µm) and texture from two samples were studied, located 340 m apart along the drillhole RU65-7976 from the NW lobe. In the first (CLC 6), pyrite is commonly rounded and sutured, featuring embayed margins against the surrounding matrix and annealing has obliterated any microscale evidence for deformation (Figure 3A). In rare grains where relict structures can be inferred, as shown in Figure 4G, extensive brittle brecciation and milling, marked by trails of the surrounding gangue, are preserved (Figure 4G). The retention of a (sub)-idiomorphic morphology that records partial deformation is evidence that this is an aggregate of pyrite.

BC and Z-IPF mapping of the aggregate confirms this and displays misorientation spatially associated with the relict trails (Figure 8A,B). Domains of gradual misorientation fabrics close to grain margins are seen clearly in the GROD angle map (Figure 8C). Pole figures in Figure 8D depict two distinct grain orientations, labelled as Py1 and Py2 on the Z-IPF map (Figure 8B). The two Py2 sub-grains share identical orientations and lie on either side of Py1 with sharp margins to the matrix. Py2 contains trails that partially correspond with those in Py1; however, the structures associated with large misorientation in Py1 (Figure 8B,E—blue transect) do not extend into Py2. This area of progressive stepwise misorientation viced between the Py2 grains preserve a shift on all <100> axis (Figure 8D) whereas the area of internal misorientation intersected by the red transect (Figure 8B,E) seems to display a rotation about a single <100> axis (Figure 8D). Gradual misorientation in Py2 exhibits a rotation about at least two <100> axis (Figure 8D).

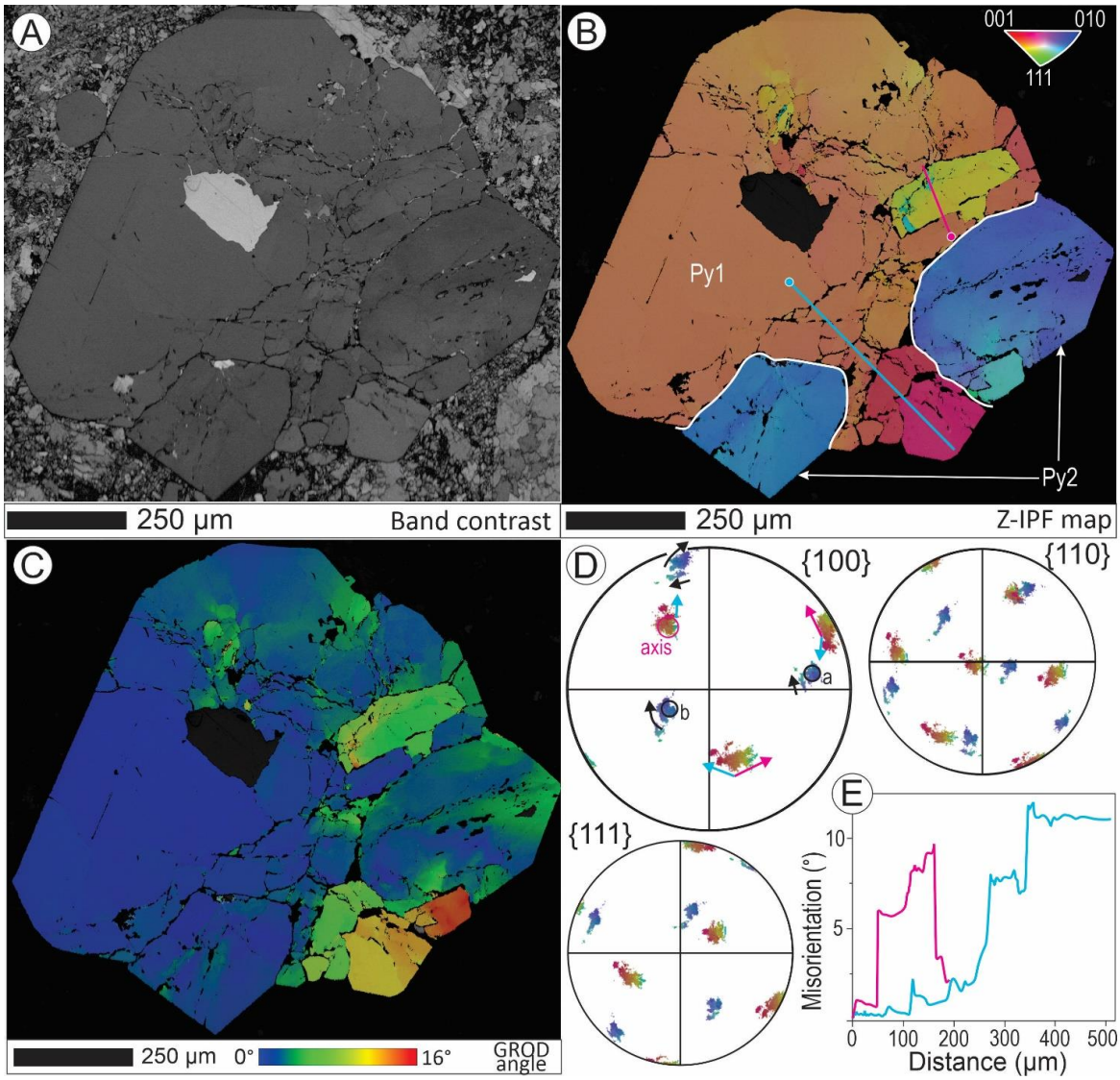

Figure 8. Orientation contrast EBSD maps and data from pyrite in sample CLC6 (Figure 4G). (**A**) BC, (**B**) Z-IPF and (**C**) GROD angle maps depicting spatial misorientation. (**D**) {100}/{110}/{111} pole figures with colors derived from (**B**). Two orientations of rotation are displayed in 'Py1′ (yellow and red on (**B**)) and shown (**E**) along transects. The pink axis rotation annotations on (**D**) correspond to the pink transect on (**B**,**E**), whereas the cyan annotations depicting a shift of all axes on (**D**) reflects the cyan transect on (**B**,**E**). 'Py2′, shown on (**B**), exhibits rotation about two axis marked a and b with black annotations on (**D**).

The pyrite depicted in Figure 9 is from a shallower level in the same drillhole (sample CLC23) and has the morphology of an angular fragment with embayed margins. This grain is located in a very fine matrix of magnetite, hematite, chalcopyrite, and gangue minerals, all of which also occur as inclusions alongside coarse, elongated pores (Figure 9A). The BC map shows no obvious orientation contrast while the GROD angle map displays gradual misorientation across the grain (Figure 9B). As in the previous sample (CLC6), the subtle marginal misorientation fabric is indicative of plastic deformation. A profile taken vertically across the grain shows an almost constant rate of misorientation (~0.1°/50 µm) that culminates at 2° (Figure 9D). Inclusions close to the top margin seem to have disrupted the lattice deformation response to some degree, but this was insufficient for dislocation formation.

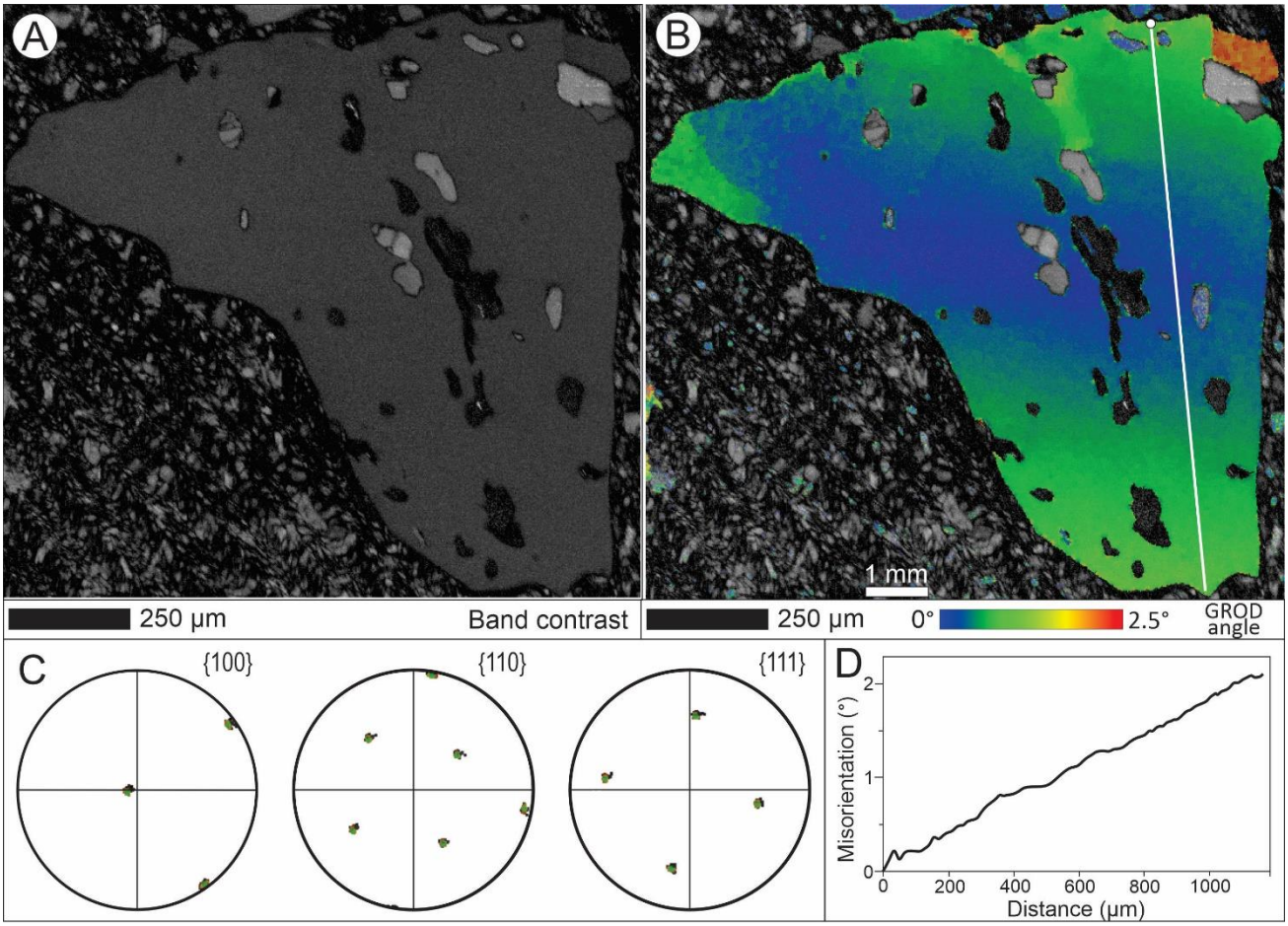

Figure 9. (**A**) BC and (**B**) GROD angle maps with associated (**C**) {100}, {110} and {111} pole figures of pyrite from sample CLC23. (**D**) A transect, with its trajectory shown in (**B**) by a white line, depicts subtle and progressive cumulative misorientation across the grain.

4.2. Interpretation of EBSD Textures

EBSD results show some pole figures that display shifts of all axes can be attributed to fracture rotation. Fracture-associated rotation is observed where there is obvious cataclasis (Figure 5C), as well as across some trails of gangue mineral inclusions (Figures 6B and 8C). We therefore infer that these gangue trails represent healed fractures (hereafter referred to as such), which were infilled by gangue and superposed by pyrite recrystallization. EBSD analysis also reveals domains that show rotation about {100} (Figures 5C, 6E, 7D and 8D) and rarely {110} (Figure 6C) axes. Lattice distortions associated with these rotations either display subtle degrees of misorientation over hundreds of µm (Figures 6B, 8C and 9B), or sudden shifts of up to 8° misorientation marked on orientation contrast maps by low- and mid-angle subgrain boundaries (Figures 6B and 7C). These match descriptions of

the ductile deformation mechanisms dislocation glide and dislocation creep respectively (e.g., [4,5,57]).

In the Distal satellite, pyrite displays no direct microstructures indicative of ductile deformation, though the pole figures do reveal an apparent axis rotation about a single <100> (Figure 5C—D1). The pole figure rotation histories can be traced back to a single orientation (Figure 5C—orange spots) that displays all grains depicted in the Figure 3D inset originally belonged to a single phenocryst. The axis rotation (Figure 5C—D1) is the first preserved deformation in this pyrite. A second deformation (D2) is recognized from a shift of all axes (Figure 5C), corresponding to brittle fracture rotation subsequent to the D1 event that progresses into randomly orientated fine grains during milling.

All pyrites, except the example from Distal satellite, display ductile microstructures irrespective of the breccia matrices in which they are hosted, i.e., (i) hematite-dominant (Figure 3A), (ii) siderite-rich (Figures 3B and 4D), and (iii) veins across quartz–chlorite domains (Figure 3C). In assemblages (i) and (ii) that are characterized by a very fine matrix and/or surrounding ductile phases (Figures 6A, 8A and 9A), marginal ductile deformation in pyrite operated primarily through dislocation glide. Dislocation creep is present in pyrite from siderite-dominated (Figure 6B) and quartz–chlorite (Figure 7C) assemblages (ii and iii above). In assemblage (ii), dislocation creep develops as a continuation of dislocation glide that, in areas of pyrite 'bottlenecking', is interrupted, favoring dislocation locking and the formation of low-angle subgrain boundaries (Figure 6B). Assemblage (iii) displays sparse marginal low- to mid-angle subgrain boundaries alongside a pulverized grain containing intact fractures (Figure 7C). This assemblage is mostly composed of coarse rigid quartz (Figure 3C) and is, thus, mechanically distinct from the hematite-dominant or siderite rich breccias.

4.3. Pyrite Trace Element Mapping

LA-ICP-MS element maps were collected on three selected pyrite grains in samples from the ODBC outer shell that had been previously mapped by EBSD.

Element mapping of the pyrite grain in sample MV18B (Figures 3B and 6) reveals the grain core is relatively enriched in Ni, Co, and Te, which is enclosed by a patchy zonation in terms of Ni, Co, and As, in which Co and Ni display an antithetic relationship (Figure 10). The patchy, imperfect zoning patterns may reflect sub-solidus diffusion in the core domain. The patchy domain is enclosed by a Co-As-rich reaction rim, which in turn displays an idiomorphic overgrowth decorated by patchy enrichment in Bi, Pb Au, and Te that is further enclosed by an outermost zone deficient in all trace elements. The medium angle subgrain that displayed rotation about a <110> (Figure 6C) is shown to be at the idiomorphic margin and displays local enrichment in Au, Ag, Te, Bi, and Pb (Figure 10). Other subgrain boundaries (Figure 6B,E) display a comparable enrichment in Au, Ag, Te, Bi, and Pb (Figure 10). Healed microfractures across the grain, including microstructure 1, show a high concentration of mobile elements: Co, As, Te, Au, Pb, Bi, and Ag. Pyrite zonation patterns are offset by microstructure 1 and, to the right, display an apparent irregular depletion in Ni spatial to observed marginal dislocation glide (Figure 6B).

Pyrite from sample MV37 (Figures 3C and 7) displays patchy zoning and overgrowths in which Ni and Co have a correlative relationship that often trends antithetical to As (Figure 11). As expected, Au also displays an association with As-rich domains but shows no correlation with Ag, Te, or Bi that would suggest inclusions containing these elements. Importantly, the low- to medium-angle subgrain boundaries have clearly offset the compositional zonation and exhibit a relative enrichment in Ni and Co (Figure 11). Other trace elements contained in the pyrite show no apparent relationship with the dislocations, while Bi and Pb, however, appear strongly enriched (Figure 11).

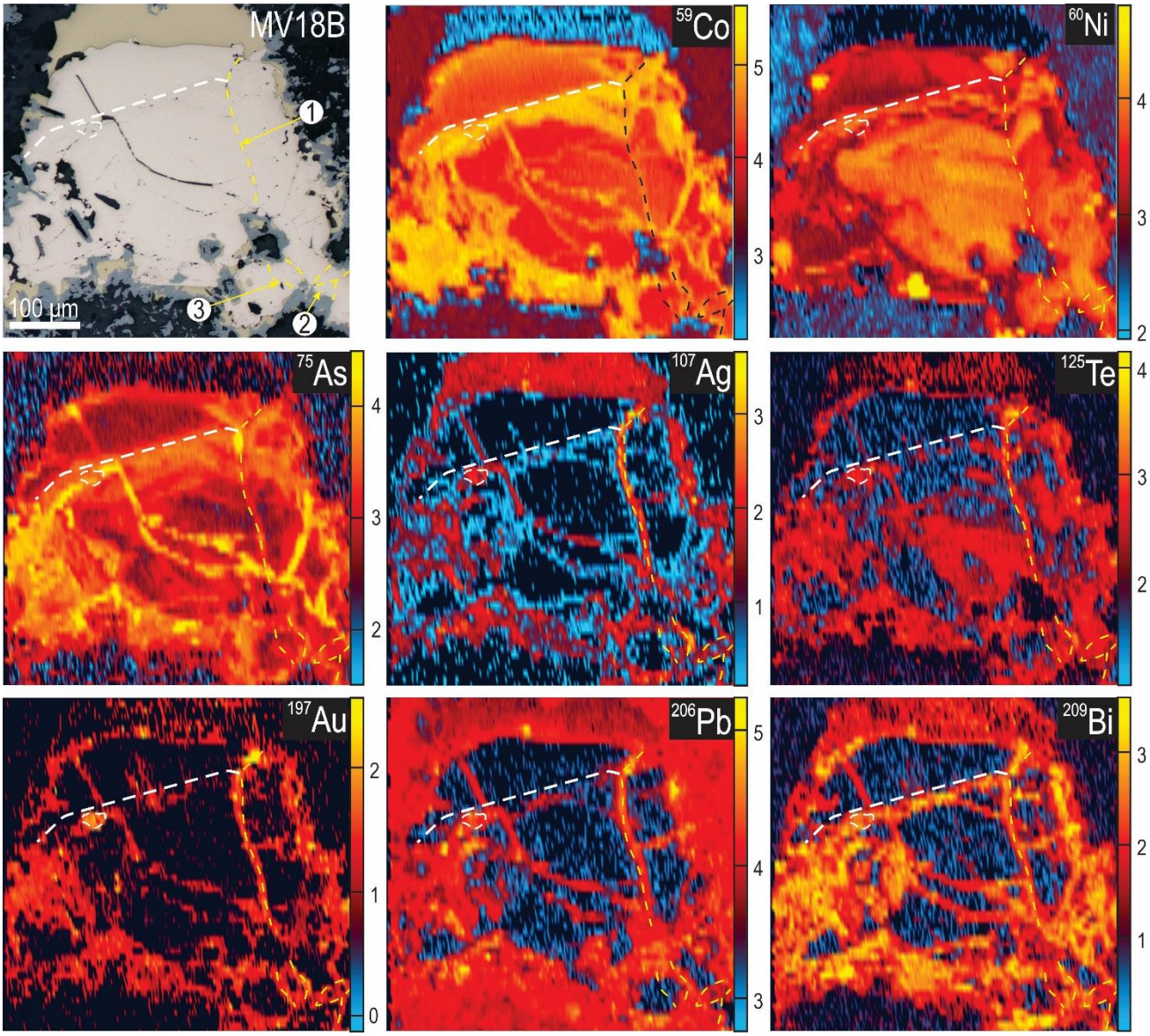

Figure 10. LA-ICP-MS maps and corresponding reflected light micrograph of pyrite grain from sample MV18B annotated with yellow dashed lines corresponding to microstructures 1, 2, 3, and the lenticular {110} domain shown by EBSD (Figure 6). Pyrite contains patchy zonation with respect to As, and antithetic Ni-Co zonation enclosed by a reaction rim relatively enriched in Co and As marked by a white dashed line. Crosscutting microstructures display elevated Co, As, Te, Au, Bi, Pb, and Ag. Scales in counts-per-second.

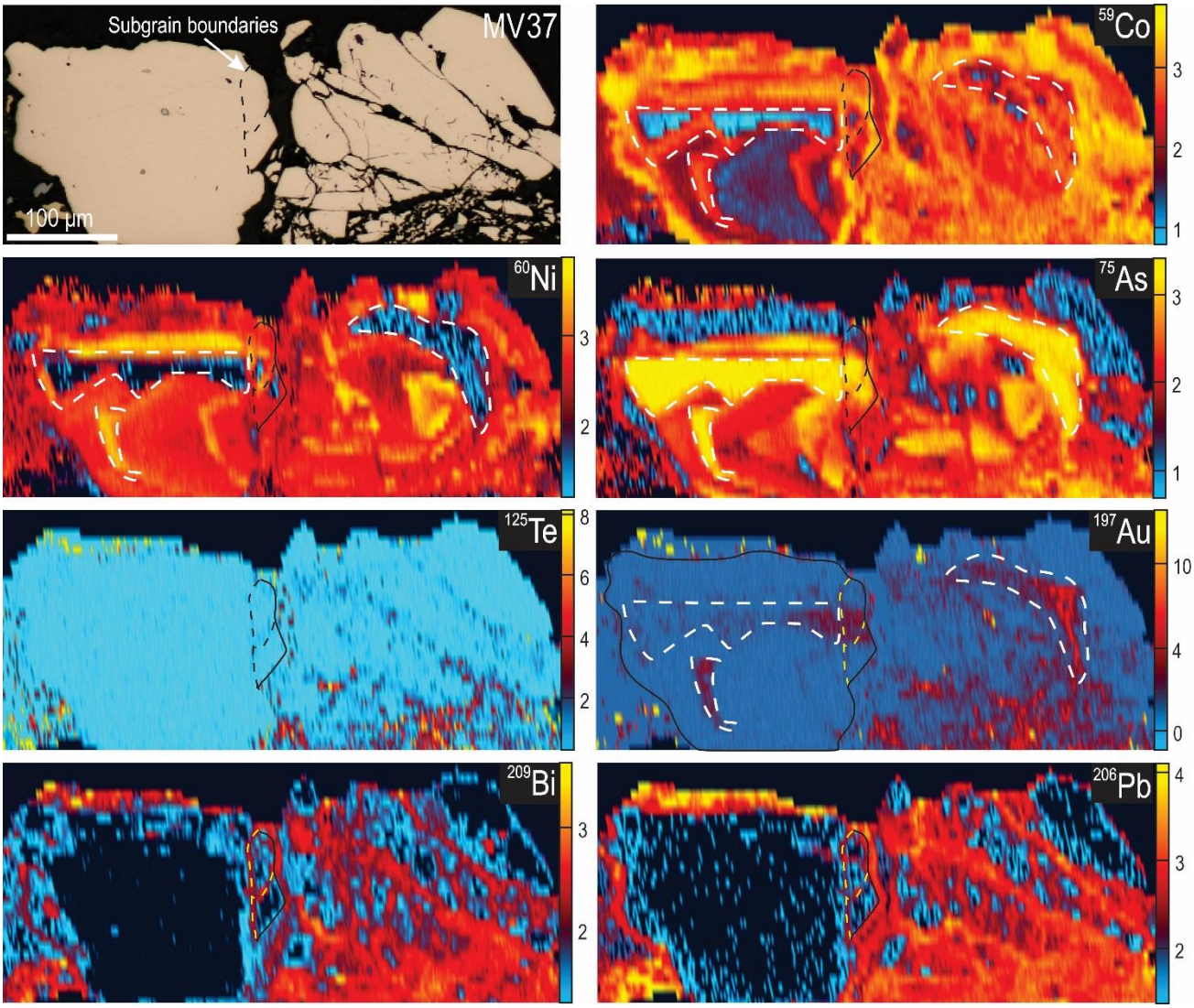

Figure 11. LA-ICP-MS maps and corresponding reflected light micrograph of pyrite grains in sample MV37 annotated with sub angle boundaries shown by EBSD (Figure 7). Pyrite shows patchy zoning with respect to Ni, Co, As, and Au annotated by white dashed lines, with yellow or black dashed lines over microstructures with relative enrichment in Bi and Pb. Scales in counts-per-second; ^{197}Au in linear scale (n × 10^0) and ^{125}Te in linear scale (n × 10^1).

Lastly, the pyrite from sample CLC6 (Figures 3A and 8) is rich in trails of gangue mineral inclusions that can be readily seen on the element maps from enhanced ^{27}Al (Figure 12). These trails display a relative enrichment of Au, Bi, Ag, Sb, Zn, Pb, Se, Ni, and As. The same elements also appear at greater concentrations in adjacent healed fractures. In parts of the pyrite grain with fewer or no inclusions, a Ni-rich preserved core is observed, in which Co and As are relatively depleted. This grain core is enclosed by oscillatory-zoned pyrite featuring bands, ~20 µm in thickness, with alternating high and low concentrations of Ni, Co, As, Te, and Se (Figure 12). The entire grain is surrounded by an irregular reaction rim that is relatively enriched in Se and As but depleted in Te, Ni, and Co (Figure 12). Marginal dislocation glide in this grain (Figure 8C) closely correlates with the Se-As rim. We draw attention to the rounded pyrite grain at the top left of the LA-ICP-MS maps. This grain displays contrasting zonation patterns in that the core is relatively enriched in Co, As, and Se, while the rim contains higher Ni.

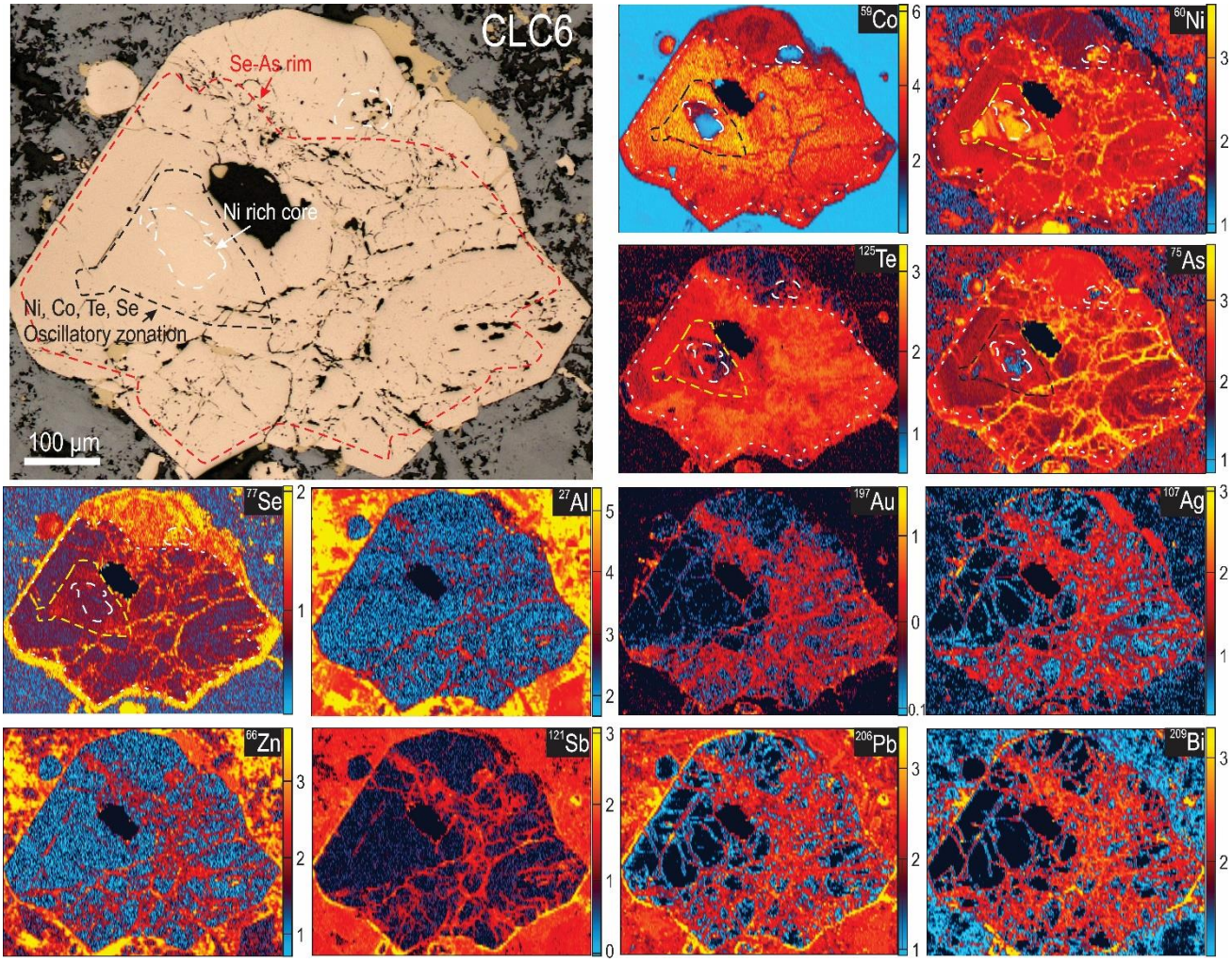

Figure 12. LA-ICP-MS maps and corresponding reflected light micrograph of pyrite grain from sample CLC6. Chemical data depicts a relict Ni-rich core, surrounding an oscillatory zonation with respect to Ni, Co, As, Te, and Se and an As-Se-enriched reaction rim. Scales in counts-per-second; ^{59}Co in linear scale (n × 10^4) and ^{77}Se in linear scale (n × 10^2).

5. Discussion

5.1. Pyrite Deformation Textures

As expected in a breccia-hosted deposit, the most conspicuous and widely reported deformational texture in pyrite across Olympic Dam is cataclasis [28,32]. The cataclastic textures observed are comparable with that described from many sulfide ore deposits [2,58] and display pyrite grain pulverization and fracture offset with subsequent particle size reduction through milling and rock flour formation. This infers prolonged brittle failure that continually acted to lessen bulk strain across the deposit.

Ductile microstructures pertaining to dislocation glide and creep are also shown here in all assemblages from the NW-SE transect, at depths ranging from ~500 m to as deep as 1850 m. Ehrig et al. [32] reported nanoscale structures (low-angle slip dislocations, twist walls, and deformation-dipole nanostructures) and used these to infer brittle-to-ductile deformation of pyrite from depths of ~1800 m in the orebody. P-T conditions were estimated at 0.5–1 kbar and 300–400 °C, in agreement with models for the mineralizing event at Olympic Dam [30,48]. The present data confirm such an interpretation as being a much wider phenomenon and is documented here for the first time at the micron-scale, in a breccia-hosted IOCG deposit.

Dislocation glide is the fundamental ductile mechanism allowing dislocations to move unhindered along a crystal lattice or glide plane in response to stress(es) (e.g., [59]). This is shown to be the dominant mechanism in the studied pyrite (Figures 6B, 8C and 9B), in which the surrounding material allows uninterrupted glide without grain locking or strain hardening which has been shown in prior studies on pyrite [4,59]. However, when 'obstacles' or 'blockages' hinder glide planes, generation of low-angle (>2°) boundaries are produced by dislocation climb [60], as we have observed in two of the four cases with ductile deformation (e.g., Figures 6B and 7C). When dislocation glide and climb combine, the phenomenon is known as dislocation creep [57].

The relatively rigid quartz from the quartz–chlorite breccia (Figure 3C) represents a mechanically different matrix compared to the other pyrites, facilitating marginal dislocation creep in response to imposition against the larger quartz (Figure 7C), a mechanism discussed for regionally metamorphosed pyrite [4,5]. This dislocation creep can be associated with the shear-induced deformation of pyrite in Figure 4F, implying ductile deformation during a fracturing event superimposed onto a pre-existing breccia. In the absence of a rigid matrix, 'bottlenecking' of a developing dislocation glide system also led to dislocation creep (Figure 6B) in pyrite from siderite-rich breccia (Figures 3B and 4D). EBSD studies of both natural and experimentally deformed pyrite have shown that dislocation creep is common down to the brittle/ductile transition at ~260 °C [3,11,13].

5.2. Pyrite Geochemistry and Syn-Deformational Geochemical Remobilization

Dmitrijeva et al. [61] used multivariate statistics to investigate geochemical trends in a relatively large dataset for pyrite from Olympic Dam. Pyrite is characterized by concentrations of As, Co, and Ni that vary across several orders of magnitude and readily attributable to grain-scale zonation. LA-ICP-MS element maps of pyrite (Figures 10–12) confirm the zonation with respect to As, Co, and Ni, while noting that the zoning is often irregular, patchy, or otherwise disrupted and overprinted, echoing prior, largely unpublished element maps (e.g., [62]). Cobalt is the most abundant trace component, ~10^5–10^4 ppm, a feature typical of hydrothermal pyrite (e.g., [18,63,64]). Cobalt, Ni, and As display only weak relationships with one another (Figures 10 and 12), and Ni and Co often show an antithetical correlation (Figure 11). In sample MV37, most As-rich domains are depleted in Co and Ni yet contain greater concentrations of Au (Figure 11). These relationships reflect a rapidly evolving ore fluid physiochemistry during formation feasibly tied to fluctuation in temperature and fluid compositions (e.g., [64]). LA-ICP-MS element mapping of pyrite from sample MV18B (Figure 10) and CLC 6 (Figure 12) displays Ni-rich relict cores. CLC 6, in particular, is most distinct, because the Ni core is also highly depleted in As, Co, Se, and Te.

The marked correlation between Ag-Bi-Pb-(Au) in Olympic Dam pyrite has been attributed to inclusions of Ag-(Au)-, Pb-, and Pb-Bi-tellurides [61]. Ehrig et al. [32] provided nanoscale evidence for such inclusions, concluding that the Ag-Bi-Pb-(Au) is likely to have been released from the pyrite lattice and remobilized on the scale of microns to millimeters. Mapped pyrites in the present study feature signatures attributable to telluride inclusions, but these are mainly found along healed microfractures with As also present (Figures 10 and 12). Hydrothermal pyrite that is poor in these metals is often invoked to have undergone episodes of reworking and recrystallization (e.g., [26,65,66]), with released trace elements either forming discrete minerals or being partitioned into other coexisting sulfides such as chalcopyrite [67,68]. Redeposition and fixing of these mobile elements in healed microfractures suggest that the reworking of pyrite was syn-deformational. Healed microfractures are largely invisible in reflected light or in BSE images but are readily seen in both EBSD and element maps. In fact, healed microfractures are ubiquitous in Olympic Dam pyrite (Figures 4D,G, 10 and 12), and probably contribute more to the overall Ag-Bi-Pb-(Au) signature of pyrite than mineral inclusions unrelated to fractures. The widespread presence of elevated radiogenic Pb along microfractures is in response to uranium decay and migration of daughter radionuclides [34].

Ductile microstructures like low- to high-angle slip dislocations and subgrain boundary domains are widely shown to accommodate a wide range of trace elements [19,21,25,26]. The micron- to nanoscale study of Ehrig et al. [32] on kin structures in pyrite from elsewhere at Olympic Dam demonstrated that Bi-Pb sulfotellurides and Ag-Au tellurides are hosted as nanoparticles alongside pore-attached nanoparticles indicative of high fluid percolation. In Figure 10 we show similar low- to medium-angle slip dislocations (Figure 6B) with Ag-Au-Pb-Bi-Te enrichment. This chemistry is analogous to that described in Ehrig et al. [32] and thus supports the same syn-deformational ductile trace element (re)mobilization model for these dislocations. The same microstructures in Figure 11 display concentrations of Pb and Bi, and minor Ni and Co remobilization despite visible Au enrichment in pyrite, suggestive of more limited release and remobilization. The LA-ICP-MS trace element maps therefore indicate a response to syn-deformation remobilization that is highly localized and varies in intensity between samples and even among different grains in the same sample. We also note depletion of Te across the grain (Figure 11) if compared to the example in Figure 10. The lack of Ag and Au (re)mobilized into these dislocations alongside the Te depletion in pyrite, may infer the importance of Te held within pyrite in the formation of nanostructural Au-Ag-tellurides, as proposed previously [32].

Marginal dislocation glide (sample MV18B; Figure 6B) correlates closely with an irregular depletion in Ni that is not reproduced by other elements (Figure 10). To the best of our knowledge, no other study has reported trace element distributions over domains of dislocation glide. Although our interpretations are preliminary and demand corroboration in the future, they suggest that dislocation glide processes have the capacity to disrupt and remobilize trace elements in pyrite, causing an order of magnitude difference in concentrations of Ni in this case. This mechanism most closely resembles dislocation-impurity pair diffusion [69], in which a gliding dislocation attracts and disrupts solid state impurities within its strain field, or 'Cottrell atmosphere' [70,71]. Domains depleted in trace elements have been attributed to Cotrell atmospheres in several prior studies [22,72,73], although dislocation glide has never been observed across the same domain.

5.3. Pyrite Deformation History—Early Stages

Textural observations in the Distal satellite are in marked contrast to those from samples selected along the NW-SE transect (e.g., Figures 6–9) that clearly record pervasive recrystallization and replacement that has resulted in wholesale obliteration of textural histories. Poor preservation of early textures and fabrics in the central ODBC is a consequence of the iron-metasomatism of initial RDG, involving pervasive replacement of igneous minerals by hematite, sericite, and chlorite [28]. The identity of the precursor granite and superimposed alteration reactions can only be resolved from the evidence preserved in RDG well outside or away from the deposit [46], where alteration is markedly weaker [74].

It is therefore implicit that the microstructural evolution of the deposit may well be better preserved in samples such as those from the Distal satellite, emphasizing the utility of such samples for constraining the early stages of IOCG evolution. Indeed, although the brecciated granite (sample MV65, Figure 3D) appears only as an initial alteration stage, pyrite records two distinct rotations (D1-2; Figure 5C,D) implying the Distal satellite was exposed to at least two deformation events. The two-phase chalcopyrite–pyrrhotite assemblage is indicative of unmixing from a higher temperature intermediate solid solution (iss; [75,76]) that is preserved as rounded inclusions (Figure 4B,C), and thus suggests that the pyrite was exposed to temperatures in excess of 557 °C [76]. This links initial pyrite mineralization to during the magmatic–hydrothermal transition [30,48]. The D1 rotation would allow inference of ductile behavior at this early stage of deposit formation, although no direct microstructures are observed to unequivocally support such a hypothesis and moreover, the 'original' orientation, prior to the two rotations (Figure 5C—orange spots) could pertain to a later replacement or recrystallization stage rather than primary pyrite. Despite this, D1 is likely a ductile rotation taking place at high temperature reached during

the early magmatic to hydrothermal transition [30,48] whereas D2 is controlled by fracture rotation at an undefined later stage.

5.4. Were All Microstructures Obliterated by Coupled Dissolution Reprecipitation Reactions?

At Olympic Dam, semi-continuous coupled dissolution reprecipitation reactions (CDRR) are invoked from the widespread observation of replacement, remobilization, and recrystallization phenomena in numerous mineral groups. Previous work on pyrite from elsewhere [4,11,77] suggests that recrystallization driven by processes such as CDRR struggles to completely erase dislocations from grains compared to recrystallization/recovery processes. As shown from Olympic Dam [78–80], however, pervasive CDRR can be sufficient to account for wholesale grain replacement and recrystallization due to the likely long-lived nature of fluid flow. EBSD mapping of pyrite grains from diverse samples during reconnaissance work for this study emphasized the lack of microstructures that could directly corroborate such an interpretation, however encouraging the macroscale textures appeared. Nonetheless, the representative pyrite assemblages from across the outer shell illustrated here as Figures 6–9 represent compelling evidence for pervasive CDRR, even if they are compiled from a select group of relatively rare examples in which annealing, and recrystallization were insufficient to erase all evidence of applied deformation. This is particularly relevant in the context of studies that recognize multiple intense fluid percolation events across diverse mineral groups from Olympic Dam and other IOCG systems in the region [32,74,81].

Despite pervasive CDR-driven replacement reactions, a succession of structural events can be postulated based on the ductile microstructures (as dislocation glide and/or creep at grain margins; Figures 6B, 7C, 8C and 9B) alongside growth textures and crosscutting fractures from pyrites along the NW-SE transect. Based on the discontinuity of dislocation glide across fractures (Figures 6B, 8C and 9B) and the association of dislocation creep relative to fragmented grains (Figure 7E), we can infer that these instances of ductile deformation are the latest preserved deformation in our selected grains and supersede fracturing.

However, early ductile deformation is evidenced by internal domains rotated about <100> or <110> axis relative to the host grain (Figures 6B,C and 8B). Such features cannot be attributed to late recrystallisation because intra-domain rotation is accommodated by the {110} slip system in pyrite (Figure 6C). This slip system is rarely activated in experimentally deformed pyrite due to its much higher critical resolved shear stress compared to the {100} [8,59,82] but can occur by grain impingement in natural pyrite [10]. Such impingement (<110> domain location at the margin of internal zonation and its bent lenticular morphology) is observed for shallow pyrite in the 'Nodular Fe-oxide granite' drillcore (Figure 6C). Furthermore, the impinged {110} domain is separated from the later marginal dislocation glide superposed by crosscutting fractures (Figure 6B), providing evidence for multi-stage, brittle-to-ductile transition events recorded in pyrite. Such interpretation is concordant with an environment that experienced periodic moderate- to high-temperature fluid flow during CDR-driven replacement reactions, recognized in minerals including pyrite at Olympic Dam.

Positioning these deformation events in time is, however, impossible at present given the uncertainties surrounding the broader structural evolution at Olympic Dam. Unravelling the evolution and assigning individual microstructures to specific events would require substantial additional study, potentially involving an integrated microstructural-geochronological approach for pyrite and co-existing minerals (e.g., magnetite, hematite, quartz, chalcopyrite, and albite). Despite this, the radioisotope record and recognition of several post ~1.6 Ga tectono-thermal events across the Olympic Cu-Au Province (Figure 1), allow us to offer some speculative scenarios.

A first consideration is South Australia's enrichment in heat producing elements (HPE) which is shown to generate anomalously elevated geothermal gradients and heat flows across the region [83]. This has produced the South Australian Heat Flow Anomaly in

which heat flow is two to three times above average and can drive high temperature–low pressure metamorphism (e.g., [83–85]). In the Yorke Peninsula, SE Gawler Craton, Bockmann et al. [85] found evidence for a metamorphic event between 1.56–1.5 Ga, thermally driven by this HPE heat anomaly at P-T conditions of 660–750 °C and 3.6–5.5 kbar. They established a geothermal gradient of 45–50 °C/km, which resembles present day measurements of the surrounding Stuart Shelf [86]. Olympic Dam is the largest single uranium deposit on Earth and consequently displays a major thermal anomaly linked to uranium decay [87]. At Olympic Dam, an average present day heat flow of 125 mW/m^2 and steep temperature gradient of 83.1 (±5.5) °C/km was recorded [86], which is ~63% higher than the surrounding South Australian Heat Flow Anomaly. If this is considered alongside a (semi-)continual supply of radiogenic heat and the semi-continuous fluid flow, as argued by Owen et al. [88], this may have allowed for long-lived rejuvenation of economic metals across the mineral system [85]. Evidence presented for secondary U enrichment at Olympic Dam [89] and the isotope systematics of carbonates [90] also indicate multiple stages of hydrothermal activity after 1 Ga.

The recognition of ductile deformation at Olympic Dam is novel for IOCG deposits and would require temperatures above ~260 °C [13], more typical of orogenic gold [6,20,21] or metamorphosed massive sulfide deposits [4,5,10]. At Olympic Dam, the primary Woodall fault of the Discovery Fault Series records >2.5–3 km of normal displacement, with later superimposed faults preserving 1 km of sinistral strike slip and an undetermined oblique aspect [49]. These structures are used to infer multiple burial and unroofing events at Olympic Dam [29,91]. The anomalous present day geothermal gradient of ~83 °C/km at Olympic Dam is sustained by radioactive decay [86,87]. Higher heat production likely existed earlier in the evolution of the deposit. If accompanied by large fault displacements and associated tectonothermal events like emplacement of the Gairdner LIP [51], sudden transition between brittle to ductile regimes would be plausible and correlates with our observation of alternating ductile and brittle deformation microstructures in pyrite. The proposed waxing and waning, effectively semi-continuous fluid flow at Olympic Dam [88] would assist this, with even small changes in burial depth generating high-temperature metamorphic fluid systems [85].

6. Conclusions

Brittle microfractures and ductile microstructures such as low- to medium-angle boundaries and subtle misorientation from dislocation glide were identified in pyrite using EBSD. Dislocation glide textures are more frequently observed and are attributable to the abundant enclosure of pyrite within softer phases (commonly chalcopyrite or siderite) or mechanically similar fine brecciated matrices. LA-ICP-MS element mapping across these microstructures displayed: (i) relative enrichment in Ag-Au-Pb-Bi-Te in low- to medium-angle boundaries; (ii) a similar enrichment along healed microfractures; and (iii) depletion of Ni, in this case, by an order of magnitude, correlating spatially with dislocation glide. All the above styles of chemical (re)mobilization are interpreted as syn-deformational in origin. Variation in chemistry between microstructures and their correspondence with trace element zoning visualized on LA-ICP-MS maps indicate that the response to deformation is highly localized and varies in intensity between grains.

This work presents the first evidence for ductile deformation in pyrite from a breccia-hosted IOCG deposit. Two stages of ductile behavior are observed in specimens from the Olympic Dam deposit. However, extensive replacement and recrystallization driven by CDRR have prevented widespread preservation of the earlier event. A combination of radioactive decay heat and adjacent tectonothermal events are invoked to account for an anomalously high geothermal gradient within and surrounding the deposit that reached temperatures of ~260 °C to enable ductile behavior in pyrite. (Re)activation of faults with large displacement in the elevated geothermal gradient supported multiple alternations between brittle to ductile regimes. The coupling of EBSD methods with LA-ICP-MS element mapping therefore provides a comprehensive characterization of

pyrite textures and microstructures that are otherwise invisible on conventional reflected light or BSE images. This data is shown to provide new insights into ore genesis and superimposed events.

7. Implications and Outlook

A radioactive heat source has operated at Olympic Dam over the past 1.6 million years and must therefore have been integral for the post-initial evolution of many mineral groups, and especially for Cu-Fe-sulfides, which can remain reactive under even mild hydrothermal conditions (e.g., [92–94]). Models of secondary evolution for Olympic Dam should therefore be updated to account for these findings. Although this study has revealed ductile deformation in pyrite and invoked mechanisms to attain the required temperature, how these events fit into the deposits structural evolution remains unclear. Future EBSD work should be directed towards grains of time-resolved pyrite and associated minerals to constrain the character and timing of individual structural brittle/ductile events. As ductile behavior in pyrite is intimately linked to fault (re)activation, findings would directly relate to tectonism across the deposit.

This study also displayed the grain-scale distribution of minor elements and how these distributions relate to textures and microstructures. A detailed understanding of this is essential to efforts aimed at recovery of value components (precious and critical metals), as well as removal of deleterious components (e.g., [35–37]). The development of low-energy, low-waste methods of ore processing, coupled with recovery of all contained elements of value, is not only linked to mineralogy and rock features at the hand specimen scale, but also to the hidden features that impact on and control rock fragmentation, separation, and recovery. Considering the long-term value of such information to the resource industry of the future, EBSD methods appear underutilized by researchers despite their demonstrated effectiveness (e.g., [6,19,25,26]).

Author Contributions: S.A.K. and N.J.C. conceived this contribution. Analytical work was performed by S.A.K., with assistance from A.B. with FIB-SEM operation and S.G. for LA-ICP-MS set-up and optimization. The manuscript was written and revised by S.A.K., N.J.C. and C.L.C., with comments and edits from K.E., Y.T.C.R., A.B. and S.G. All authors have read and agreed to the published version of the manuscript.

Funding: This study was funded by Australian Research Council Linkage grant LP200100156 to N.J.C. and K.E, co-supported by BHP Olympic Dam.

Data Availability Statement: Datasets are available from the corresponding author upon request.

Acknowledgments: Benjamin Wade and Ken Neubauer (Adelaide Microscopy) are thanked for their technical support in EBSD analysis and sample preparation. We appreciate constructive comments from two reviewers.

Conflicts of Interest: Author Kathy Ehrig is employed by BHP Olympic Dam. The remaining authors declare that the research was conducted in the absence of any commercial or financial relationships that could be construed as a potential conflict of interest.

References

1. Prior, D.J.; Boyle, A.P.; Brenker, F.; Cheadle, M.C.; Day, A.; Lopez, G.; Peruzzi, L.; Potts, G.; Reddy, S.; Spiess, R. The application of electron backscatter diffraction and orientation contrast imaging in the SEM to textural problems in rocks. *Am. Mineral.* **1999**, *84*, 1741–1759.
2. Craig, J.R.; Vokes, F.M. The metamorphism of pyrite and pyritic ores: An overview. *Mineral. Mag.* **1993**, *57*, 3–18. [CrossRef]
3. Freitag, K.; Boyle, A.P.; Nelson, E.; Hitzman, M.; Churchill, J.; Lopez-Pedrosa, M. The use of electron backscatter diffraction and orientation contrast imaging as tools for sulphide textural studies: Example from the Greens Creek deposit (Alaska). *Miner. Depos.* **2004**, *39*, 103–113.
4. Barrie, C.D.; Boyle, A.P.; Cook, N.J.; Prior, D.J. Pyrite deformation textures in the massive sulfide ore deposits of the Norwegian Caledonides. *Tectonophysics* **2010**, *483*, 269–286. [CrossRef]
5. Barrie, C.D.; Cook, N.J.; Boyle, A.P. Textural variation in the pyrite-rich ore deposits of the Røros district, Trondheim Region, Norway: Implications for pyrite deformation mechanisms. *Mineral. Depos.* **2010**, *45*, 51–68. [CrossRef]

6. Li, Q.; Song, H.; Chi, G.; Zhang, G.; Xu, Z. Genesis of visible gold in pyrite in the Zhaoxian gold deposit, Jiaodong gold province, China: Constraints from EBSD micro-structural and LA-ICP-MS elemental analyses. *Ore Geol. Rev.* **2021**, *139*, 104591. [CrossRef]
7. Graf, J.L.; Skinner, B.J.; Bras, J.; Fagot, M.; Levade, C.; Couderc, J.J. Transmission electron microscopic observation of plastic deformation in experimentally deformed pyrite. *Econ. Geol.* **1981**, *76*, 738–742. [CrossRef]
8. Cox, S.; Etheridge, M.; Hobbs, B. The experimental ductile deformation of polycrystalline and single crystal pyrite. *Econ. Geol.* **1981**, *76*, 2105–2117. [CrossRef]
9. Levade, C.; Couderc, J.; Bras, J.; Fagot, M. Transmission electron microscopy study of experimentally deformed pyrite. *Philos. Mag. A* **1982**, *46*, 307–325. [CrossRef]
10. Boyle, A.; Prior, D.; Banham, M.; Timms, N. Plastic deformation of metamorphic pyrite: New evidence from electron-backscatter diffraction and forescatter orientation-contrast imaging. *Miner. Depos.* **1988**, *34*, 71–81. [CrossRef]
11. Barrie, C.D.; Boyle, A.P.; Prior, D.J. An analysis of the microstructures developed in experimentally deformed polycrystalline pyrite and minor sulphide phases using electron backscatter diffraction. *J. Struct. Geol.* **2007**, *29*, 1494–1511. [CrossRef]
12. Barrie, C.D.; Boyle, A.; Salter, M. How low can you go? Extending downwards the limits of plastic deformation in pyrite. *Mineral. Mag.* **2009**, *73*, 895–913. [CrossRef]
13. Barrie, C.D.; Pearce, M.A.; Boyle, A.P. Reconstructing the pyrite deformation mechanism map. *Ore Geol. Rev.* **2011**, *39*, 265–276. [CrossRef]
14. Large, R.R.; Danyushevsky, L.; Hollit, C.; Maslennikov, V.; Meffre, S.; Gilbert, S.; Bull, S.; Scott, R.; Emsbo, P.; Thomas, H.; et al. Gold and Trace Element Zonation in Pyrite Using a Laser Imaging Technique: Implications for the Timing of Gold in Orogenic and Carlin-Style Sediment-Hosted Deposits. *Econ. Geol.* **2009**, *104*, 635–668. [CrossRef]
15. Zhao, H.-X.; Frimmel, H.E.; Jiang, S.-Y.; Dai, B.-Z. LA-ICP-MS trace element analysis of pyrite from the Xiaoqinling gold district, China: Implications for ore genesis. *Ore Geol. Rev.* **2011**, *43*, 142–153. [CrossRef]
16. Cook, N.J.; Ciobanu, C.L.; Meria, D.; Silcock, D.; Wade, B. Arsenopyrite-pyrite association in an orogenic gold ore: Tracing mineralization history from textures and trace elements. *Econ. Geol.* **2013**, *108*, 1273–1283. [CrossRef]
17. Reich, M.; Deditus, A.; Chryssoulis, S.; Li, J.-W.; Ma, C.-Q.; Parada, M.A.; Barra, F.; Mittermayr, F. Pyrite as a record of hydrothermal fluid evolution in a porphyry copper system: A SIMS/EMPA trace element study. *Geochim. Cosmochim. Acta* **2013**, *104*, 42–62. [CrossRef]
18. Large, R.R.; Maslennikov, V.V. Invisible gold paragenesis and geochemistry in pyrite from orogenic and sediment-hosted gold deposits. *Minerals* **2020**, *10*, 339. [CrossRef]
19. Fougerouse, D.; Micklethwaite, S.; Halfpenny, A.; Reddy, S.M.; Cliff, J.B.; Martin, L.A.; Kilburn, M.; Guagliardo, P.; Ulrich, S. The golden ark: Arsenopyrite crystal plasticity and the retention of gold through high strain and metamorphism. *Terra Nova* **2016**, *28*, 181–187. [CrossRef]
20. Fougerouse, D.; Reddy, S.M.; Aylmore, M.; Yang, L.; Guagliardo, P.; Saxey, D.W.; Rickard, W.D.A.; Timms, N. A new kind of invisible gold in pyrite hosted in deformation-related dislocations. *Geology* **2021**, *49*, 1225–1229. [CrossRef]
21. Dubosq, R.; Lawley, C.J.M.; Rogowitz, A.; Schneider, D.A.; Jackson, S. Pyrite deformation and connections to gold mobility: Insight from micro-structural analysis and trace element mapping. *Lithos* **2018**, *310–311*, 86–104. [CrossRef]
22. Dubosq, R.; Rogowitz, A.; Sparwasser, K.; Gault, B.; Schenider, D.A. A 2D and 3D Nanostructural Study of Naturally Deformed Pyrite: Assessing the Links Between Trace Element Mobility and Defect Structures. *Contrib. Mineral. Petrol.* **2019**, *174*, 72. [CrossRef]
23. Börner, F.; Keith, M.; Fougerouse, D.; Macauley, C.; Felfer, P.; Yokosawa, T.; Zubiri, B.A.; Spiecker, E. Between defects and inclusions: The fate of tellurium in pyrite. *Chem. Geol.* **2023**, *635*, 121633. [CrossRef]
24. Abramovich, M.G.; Shmakin, B.M.; Tauson, V.L.; Akimov, V.V. Mineral typochemistry: Anomalous trace-element concentrations in solid solutions with defect structures. *Internat. Geol. Rev.* **1990**, *32*, 608–615. [CrossRef]
25. Reddy, S.M.; Hough, R.M. Microstructural evolution and trace element mobility in Witwatersrand pyrite. *Contrib. Mineral. Petrol.* **2013**, *166*, 1269–1284. [CrossRef]
26. Yesares, L.; Piña, R.; González-Jiménez, J.M.; Sáez, R.; Ruíz de Almodóvar, G.; Fanlo, I.; Manuel Pons, J.; Vega, R. Distribution of critical metals in evolving pyrite from massive sulfide ores of the Iberian Pyrite Belt. *Ore Geol. Rev.* **2023**, *153*, 105275. [CrossRef]
27. BHP 2022. Annual Report 2022. Available online: https://www.bhp.com/investors/annual-reporting/annual-report-2022 (accessed on 6 November 2023).
28. Ehrig, K.; McPhie, J.; Kamenetsky, V.S. Geology and mineralogical zonation of the Olympic Dam iron oxide Cu–U–Au–Ag deposit, South Australia. In *Geology and Genesis of Major Copper Deposits and Districts of the World, a Tribute to Richard Sillitoe*; Hedenquist, J.W., Harris, M., Camus, F., Eds.; Society of Economic Geologists: Littleton, CO, USA, 2012; Volume 16, pp. 237–268.
29. Reid, A. The Olympic Cu-Au Province, Gawler Craton: A review of the lithospheric architecture, geodynamic setting, alteration systems, cover successions and prospectivity. *Minerals* **2019**, *9*, 371. [CrossRef]
30. Courtney-Davies, L.; Ciobanu, C.L.; Tapster, S.R.; Cook, N.J.; Ehrig, K.; Crowley, J.L.; Verdugo-Ihl, M.R.; Wade, B.P.; Condon, D.J. Opening the magmatic-hydrothermal window: High precision U-Pb geochronology of the Mesoproterozoic Olympic Dam Cu-U-Au-Ag deposit, South Australia. *Econ. Geol.* **2020**, *115*, 1855–1870. [CrossRef]
31. Ciobanu, C.L.; Cook, N.J.; Ehrig, K. Ore minerals down to the nanoscale: Cu-(Fe)-sulphides from the iron oxide copper gold deposit at Olympic Dam, South Australia. *Ore Geol. Rev.* **2017**, *81*, 1218–1235. [CrossRef]

32. Ehrig, K.; Ciobanu, C.L.; Verdugo-Ihl, M.R.; Dmitrijeva, M.; Cook, N.J.; Slattery, A. Lifting the cloak of invisibility: Gold in pyrite from the Olympic Dam Cu-U-Au-Ag deposit, South Australia. *Am. Mineral.* **2023**, *108*, 259–276. [CrossRef]
33. Macmillan, E.; Ciobanu, C.L.; Ehrig, K.; Cook, N.J.; Pring, A. Chemical zoning and lattice distortion in uraninite from Olympic Dam, South Australia. *Am. Mineral.* **2016**, *101*, 2351–2354. [CrossRef]
34. Rollog, M.; Cook, N.J.; Guagliardo, P.; Ehrig, K.; Kilburn, M. Radionuclide distributions in Olympic Dam copper concentrates: The significance of minor hosts, incorporation mechanisms, and the role of mineral surfaces. *Miner. Eng.* **2020**, *148*, 106–176. [CrossRef]
35. Babedi, L.; Adie, M.; Neethling, P.; Von der Heyden, B.P. A fundamental assessment of the impacts of cation (Cd, Co, Fe) substitution on the molecular chemistry and surface reactivity of sphalerite. *Miner. Eng.* **2021**, *160*, 106695. [CrossRef]
36. Can, İ.; Özçelik, S.; Ekmekçi, Z. Effects of Pyrite Texture on Flotation Performance of Copper Sulfide Ores. *Minerals* **2021**, *11*, 1218. [CrossRef]
37. Jefferson, M.; Yenial-Arslan, U.; Evans, C.; Curtis-Morar, C.; O'Donnell, R.; Parbhakar-Fox, A.; Forbes, E. Effect of pyrite textures and composition on flotation performance: A review. *Miner. Eng.* **2023**, *201*, 108234. [CrossRef]
38. Skirrow, R.G.; Bastrakov, E.N.; Barovich, K.; Fraser, G.L.; Creaser, R.A.; Fanning, C.M.; Raymond, O.L.; Davidson, G.J. Timing of iron oxide Cu-Au-(U) hydrothermal activity and Nd isotope constraints on metal sources in the Gawler craton, South Australia. *Econ. Geol.* **2007**, *102*, 1441–1470. [CrossRef]
39. Jagodzinski, E.A.; Reid, A.J.; Crowley, J.L.; Wade, C.E.; Curtis, S. Precise zircon U-Pb dating of the Mesoproterozoic Gawler large igneous province, South Australia. *Results Geochem.* **2023**, *10*, 100020. [CrossRef]
40. Flint, R.B.; Blissett, A.H.; Conor, C.H.H.; Cowley, W.M.; Cross, K.C.; Creaser, R.A.; Daly, S.J.; Krieg, G.W.; Major, R.B.; Teale, G.S.; et al. Mesoproterozoic. In *The Geology of South Australia I. The Precambrian*; Drexel, J.F., Preiss, W.V., Parker, A.J., Eds.; Geological Survey of South Australia Bulletin 54: Adelaide, Australia, 1993; pp. 106–169.
41. Allen, S.; McPhie, L.; Ferris, J.; Simpson, C. Evolution and architecture of a large felsic igneous province in western Laurentia: The 1.6 Ga Gawler Range Volcanics, South Australia. *J. Volcanol. Geotherm. Res.* **2008**, *172*, 132–147. [CrossRef]
42. Jagodzinski, E.A. Compilation of SHRIMP U-Pb geochronological data Olympic Domain, Gawler Craton, South Australia, 2001-2003. Record 2005/20. *Geosci. Aust. Canberra* **2005**, *211*, 197.
43. Cowley, W.; Conor, C.; Zang, W. New and revised Proterozoic stratigraphic units on northern Yorke Peninsula. *MESA J.* **2003**, *29*, 46–58.
44. Reeve, J.S.; Cross, K.C.; Smith, R.N.; Oreskes, N. Olympic Dam copper-uranium-gold-silver deposit. In *Geology of the Mineral Deposits of Australia and Papua New Guinea*; Hughes, F.E., Ed.; Australasian Institute of Mining and Metallurgy: Carlton, VIC, Australia, 1990; Volume 14, pp. 1009–1035.
45. Creaser, R.A. Petrogenesis of a Mesoproterozoic quartz latite-granitoid suite from the Roxby Downs area, South Australia. *Precambr. Res.* **1996**, *79*, 371–394. [CrossRef]
46. Mauger, A.J.; Ehrig, K.; Kontonikas-Charos, A.; Ciobanu, C.L.; Cook, N.J.; Kamenetsky, V.S. Alteration at the Olympic Dam IOCG–U deposit: Insights into distal to proximal feldspar and phyllosilicate chemistry from infrared reflectance spectroscopy. *Austral. J. Earth Sci.* **2016**, *63*, 959–972.
47. Kontonikas-Charos, A.; Ciobanu, C.L.; Cook, N.J.; Ehrig, K.; Kreneta, S.; Kamenetsky, V.S. Feldspar evolution in the Roxby Downs granite, host to Fe-oxide cu-au-(U) mineralisation at Olympic dam, South Australia. *Ore Geol. Rev.* **2017**, *80*, 838–859. [CrossRef]
48. Verdugo-Ihl, M.R.; Ciobanu, C.L.; Cook, N.J.; Ehrig, K.; Courtney-Davies, L. Defining early stages of IOCG systems: Evidence from iron oxides in the outer shell of the Olympic Dam deposit, South Australia. *Miner. Depos.* **2020**, *55*, 429–452. [CrossRef]
49. Clark, J. Syn-to post-mineralization structural dismemberment of the Olympic Dam Fe Oxide- Cu-U-Au-Ag Deposit. Abstract and poster. In Proceedings of the Society of Economic Geologists Conference, Keystone, CO, USA, 22–25 September 2018.
50. Betts, P.G.; Valenta, R.K.; Finlay, J. Evolution of the Mount Woods Inlier, northern Gawler Craton, Southern Australia: An integrated structural and aeromagnetic analysis. *Tectonophysics* **2003**, *366*, 83–111. [CrossRef]
51. Huang, Q.; Kamenetsky, V.; McPhie, J.; Ehrig, K.; Meffre, S.; Maas, R.; Thompson, J.; Kamenetsky, M.; Chambefort, I.; Apukhtina, O.; et al. Neoproterozoic (ca. 820–830 Ma) mafic dykes at Olympic Dam, South Australia: Links with the Gairdner Large Igneous Province. *Precambr. Res.* **2015**, *271*, 160–172. [CrossRef]
52. Preiss, W. The Adelaide Geosyncline of South Australia and its significance in Neoproterozoic continental reconstruction. *Precambr. Res.* **2000**, *100*, 21–63. [CrossRef]
53. Foden, J.; Elburg, M.A.; Dougherty-Page, J.; Burtt, A. The timing and duration of the Delamerian Orogeny: Correlation with the Ross Orogen and implications for Gondwana assembly. *J. Geol.* **2006**, *114*, 189–210. [CrossRef]
54. Ehrig, K.; Kamenetsky, V.S.; McPhie, J.; Cook, N.J.; Ciobanu, C.L. Olympic Dam iron oxide Cu-U-Au-Ag deposit. In *Australian Ore Deposits*; Phillips, G.N., Ed.; The Australasian Institute of Mining and Metallurgy: Melbourne, VIC, Australia, 2017; pp. 601–610.
55. Belousov, I.; Danyushevsky, L.; Goemann, K.; Gilbert, S.; Olin, P.; Thompson, J.; Lounejeva, E.; Garbe-Schönberg, D. STDGL3, a reference material for analysis of sulfide minerals by Laser Ablation ICP-MS: An assessment of matrix effects and the impact of laser wavelengths and pulse widths. *Geostand. Geoanal. Res.* **2023**, *47*, 493–508. [CrossRef]
56. Paton, C.; Hellstrom, J.; Paul, B.; Woodhead, J.; Hergt, J. Iolite: Freeware for the visualisation and processing of mass spectrometric data. *J. Anal. Atom. Spectrom.* **2011**, *26*, 2508–2518. [CrossRef]
57. Passchier, C.W.; Trouw, R.A.J. *Microtectonics*; Springer Science & Business Media: Berlin/Heidelberg, Germany, 2005.
58. Craig, J.R. Ore-mineral textures and the tales they tell. *Can. Mineral.* **2001**, *39*, 937–956. [CrossRef]

59. Cox, S. Flow mechanisms in sulphide minerals. *Ore Geol. Rev.* **1987**, *2*, 133–171. [CrossRef]
60. Raleigh, C.B. Glide Mechanisms in Experimentally Deformed Minerals. *Science* **1965**, *150*, 739–741. [CrossRef] [PubMed]
61. Dmitrijeva, M.; Cook, N.J.; Ehrig, K.; Ciobanu, C.L.; Metcalfe, A.V.; Kamenetsky, M.; Kamenetsky, V.S.; Gilbert, S. Multivariate statistical analysis of trace elements in pyrite: Prediction, bias and artefacts in defining mineral signatures. *Minerals* **2020**, *10*, 61. [CrossRef]
62. Ciobanu, C.L. Cu(Fe)-Sulphides from Olympic Dam; Unpublished report prepared for BHP Billiton: M 2014.
63. Huston, D.L.; Sie, S.H.; Suter, G.F.; Cooke, D.R.; Both, R.A. Trace elements in sulfide minerals from eastern Australian volcanic-hosted massive sulfide deposits; Part I, Proton microprobe analyses of pyrite, chalcopyrite, and sphalerite. *Econ. Geol.* **1995**, *90*, 1167–1196. [CrossRef]
64. Steadman, J.A.; Large, R.R.; Olin, P.H.; Danyushevsky, L.V.; Meffre, S.; Huston, D.; Fabris, A.; Listitsin, V.; Wells, T. Pyrite trace element behavior in magmatic-hydrothermal environments: An LA-ICPMS imaging study. *Ore Geol. Rev.* **2021**, *128*, 103878. [CrossRef]
65. Hannington, M.D.; Barrie, C.T.; Bleeker, W. The Giant Kidd Creek Volcanogenic Massive Sulfide Deposit, Western Abitibi Subprovince, Canada: Summary and Synthesis. *Soc. Econ. Geol. Monogr. Ser.* **1999**, *10*, 1–30.
66. Yuan, B.; Yu, H.; Yang, Y.; Zhao, Y.; Yang, J.; Xu, Y.; Lin, Z.; Tang, X. Zone refinement related to the mineralization process as evidenced by mineralogy and element geochemistry in a chimney fragment from the Southwest Indian Ridge at 49.6°E. *Chem. Geol.* **2018**, *482*, 46–60. [CrossRef]
67. George, L.L.; Cook, N.J.; Ciobanu, C.L. Partitioning of trace elements in co-crystallized sphalerite–galena–chalcopyrite hydrothermal ores. *Ore Geol. Rev.* **2016**, *77*, 97–116. [CrossRef]
68. George, L.L.; Cook, N.J.; Crowe, B.B.; Ciobanu, C.L. Trace elements in hydrothermal chalcopyrite. *Mineral. Mag.* **2018**, *82*, 59–88. [CrossRef]
69. Petukhov, B.; Klyuchnik, P. Dynamic interaction of dislocations with impurity subsystem in crystalline materials. *Crystallogr. Rep.* **2012**, *57*, 388–392. [CrossRef]
70. Cottrell, A.H. Theory of dislocations. *Prog. Phys. Met.* **1953**, *4*, 205–264. [CrossRef]
71. Cottrell, A.H.; Bilby, B.A. Dislocation theory of yielding and strain ageing of iron. *Proc. Phys. Soc.* **1949**, *A62*, 49. [CrossRef]
72. Piazolo, S.; La Fontaine, A.; Trimby, P.; Harley, S.; Yang, L.; Armstrong, R.; Cairney, J.M. Deformation-induced trace element redistribution in zircon revealed using atom probe tomography. *Nat. Comms.* **2016**, *7*, 10490. [CrossRef] [PubMed]
73. Fougerouse, D.; Reddy, S.M.; Kirkland, C.L.; Saxey, D.W.; Rickard, W.D.; Hough, R.M. Time-resolved, defect-hosted, trace element mobility in deformed Witwatersrand pyrite. *Geosci. Front.* **2019**, *10*, 55–63. [CrossRef]
74. Krneta, S.; Ciobanu, C.L.; Cook, N.J.; Ehrig, K.; Kontonikas-Charos, A. Rare earth element behaviour in apatite from the Olympic Dam Cu–U–Au–Ag deposit, South Australia. *Minerals* **2017**, *7*, 135. [CrossRef]
75. Yund, R.A.; Kullerud, G. Thermal stability of assemblages in the Cu—Fe—S system. *J. Petrol.* **1966**, *7*, 454–488. [CrossRef]
76. Cabri, L.J. New data on phase relations in the Cu-Fe-S system. *Econ. Geol.* **1973**, *68*, 443–454. [CrossRef]
77. Craig, J.R.; Vokes, F.M.; Solberg, T.N. Pyrite: Physical and chemical textures. *Miner. Depos.* **1998**, *34*, 82–101. [CrossRef]
78. Ciobanu, C.L.; Wade, B.P.; Cook, N.J.; Schmidt Mumm, A.; Giles, D. Uranium-bearing hematite from the Olympic Dam Cu–U–Au deposit, South Australia: A geochemical tracer and reconnaissance Pb–Pb geochronometer. *Precambr. Res.* **2013**, *238*, 129–147. [CrossRef]
79. Macmillan, E.; Ciobanu, C.L.; Ehrig, K.; Cook, N.J.; Pring, A. Replacement of uraninite by bornite via coupled dissolution-reprecipitation: Evidence from texture and microstructure. *Can. Mineral.* **2016**, *54*, 1369–1383. [CrossRef]
80. Verdugo-Ihl, M.R.; Ciobanu, C.L.; Cook, N.J.; Ehrig, K.J.; Courtney-Davies, L.; Gilbert, S. Textures and U-W-Sn-Mo signatures in hematite from the Olympic Dam Cu-U-Au-Ag deposit, South Australia: Defining the archetype for IOCG deposits. *Ore Geol. Rev.* **2017**, *91*, 173–195. [CrossRef]
81. Owen, N.D.; Ciobanu, C.L.; Cook, N.J.; Slattery, A.; Basak, A. Nanoscale study of clausthalite-bearing symplectites in Cu-Au-(U) ores: Implications for ore genesis. *Minerals* **2018**, *8*, 67. [CrossRef]
82. Barrie, C.D.; Boyle, A.P.; Cox, S.F.; Prior, D.J. Slip systems and critical resolved shear stress in pyrite: An electron backscatter diffraction (EBSD) investigation. *Mineral. Mag.* **2008**, *72*, 1181–1199. [CrossRef]
83. McLaren, S.; Sandiford, M.; Hand, M.; Neumann, N.; Wyborn, L.; Bastrakova, I. The hot southern continent: Heat flow and heat production in Australian Proterozoic terranes. *Spec. Pap. Geol. Soc. Am.* **2003**, *22*, 151–161.
84. De Vries Van Leeuwen, A.T.; Hand, M.; Morrissey, L.J.; Raimondo, T. Th–U powered metamorphism: Thermal consequences of a chemical hotspot. *J. Metamor. Geol.* **2021**, *39*, 541–565. [CrossRef]
85. Bockmann, M.J.; Hand, M.; Morrissey, L.J.; Payne, J.L.; Hasterok, D.; Teale, G.; Conor, C. Punctuated geochronology within a sustained high-temperature thermal regime in the southeastern Gawler Craton. *Lithos* **2022**, *430–431*, 106860. [CrossRef]
86. Houseman, G.A.; Cull, J.P.; Muir, P.M.; Paterson, H.L. Geothermal signatures and uranium ore deposits on the Stuart Shelf of South Australia. *Geophysics* **1989**, *54*, 158–170. [CrossRef]
87. Neumann, N.; Sandiford, M.; Foden, J. Regional geochemistry and continental heat flow: Implications for the origin of the South Australian heat flow anomaly. *Earth Plan. Sci. Lett.* **2000**, *183*, 107–120. [CrossRef]
88. Owen, N.D.; Cook, N.J.; Ram, R.; Brugger, J.; Maas, R.; Schmandt, D.S.; Ciobanu, C.L. Pb-bearing Cu-(Fe)-sulfides: Evidence for continuous hydrothermal activity in the northern Olympic Cu-Au Province, South Australia. *Precambr. Res.* **2023**, *398*, 107225. [CrossRef]

89. Ehrig, K.; Kamenetsky, V.S.; McPhie, J.; Macmillan, E.; Thompson, J.; Kamenetsky, M.; Maas, R. Staged formation of the supergiant Olympic Dam uranium deposit, Australia. *Geology* **2021**, *49*, 1312–1316. [CrossRef]
90. Maas, R.; Apukhtina, O.B.; Kamenetsky, V.S.; Ehrig, K.; Sprung, P.; Münker, C. Carbonates at the supergiant Olympic Dam Cu-U-Au-Ag deposit, South Australia part 2: Sm-Nd, Lu-Hf and Sr-Pb isotope constraints on the chronology of carbonate deposition. *Ore Geol. Rev.* **2022**, *140*, 103745. [CrossRef]
91. McPhie, J.; Orth, K.; Kamenetsky, V.; Kamenetsky, M.; Ehrig, K. Characteristics, origin and significance of Mesoproterozoic bedded clastic facies at the Olympic Dam Cu–U–Au–Ag deposit, South Australia. *Precambr. Res.* **2016**, *276*, 85–100. [CrossRef]
92. Li, K.; Brugger, J.; Pring, A. Exsolution of chalcopyrite from bornite-digenite solid solution: An example of a fluid-driven back-replacement reaction. *Miner. Depos.* **2018**, *53*, 903–908. [CrossRef]
93. Chaudhari, A.; Brugger, J.; Ram, R.; Chowdhury, P.; Etschmann, B.; Guagliardo, P.; Xia, F.; Pring, A.; Gervinskas, G.; Liu, A.; et al. Synchronous solid-state diffusion, dissolution-reprecipitation, and recrystallization leading to isotopic resetting: Insights from chalcopyrite replacement by copper sulfides. *Geochim. Cosmochim. Acta* **2022**, *331*, 48–68.
94. Adegoke, I.A.; Xia, F.; Deditius, A.P.; Pearce, M.A.; Roberts, M.P.; Brugger, J. A new mode of mineral replacement reactions involving the synergy between fluid-induced solid state diffusion and dissolution-reprecipitation: A case study of the replacement of bornite by copper sulphides. *Geochim. Cosmochim. Acta* **2022**, *330*, 165–190. [CrossRef]